

THE SPATIAL CLUSTERING OF *ROSAT* ALL-SKY SURVEY ACTIVE GALACTIC NUCLEI IV. MORE MASSIVE BLACK HOLES RESIDE IN MORE MASSIVE DARK MATTER HALOS

MIRKO KRUMPE^{1,2,3,4}, TAKAMITSU MIYAJI^{5,3}, BERND HUSEMANN^{2,1}, NIKOS FANIDAKIS⁶, ALISON L. COIL³, AND HECTOR ACEVES⁵

Draft version September 12, 2018

ABSTRACT

This is the fourth paper in a series that reports on our investigation of the clustering properties of active galactic nuclei (AGNs) identified in the *ROSAT* All-Sky Survey (RASS) and Sloan Digital Sky Survey (SDSS). In this paper we investigate the cause of the X-ray luminosity dependence of the clustering of broad-line, luminous AGNs at $0.16 < z < 0.36$. We fit the H α line profile in the SDSS spectra for all X-ray and optically selected broad-line AGNs, determine the mass of the supermassive black hole (SMBH), M_{BH} , and infer the accretion rate relative to Eddington (L/L_{EDD}). Since M_{BH} and L/L_{EDD} are correlated, we create AGN subsamples in one parameter while maintaining the same distribution in the other parameter. In both the X-ray and optically selected AGN samples, we detect a weak clustering dependence with M_{BH} and no statistically significant dependence on L/L_{EDD} . We find a difference of up to 2.7σ when comparing the objects that belong to the 30% least and 30% most massive M_{BH} subsamples, in that luminous broad-line AGNs with more massive black holes reside in more massive parent dark matter halos at these redshifts. These results provide evidence that higher accretion rates in AGNs do not necessarily require dense galaxy environments, in which more galaxy mergers and interactions are expected to channel large amounts of gas onto the SMBH. We also present semianalytic models that predict a positive M_{DMH} dependence on M_{BH} , which is most prominent at $M_{\text{BH}} \sim 10^{8-9} M_{\odot}$.

Subject headings: galaxies: active – cosmology: large-scale structure of universe – X-rays: galaxies

1. INTRODUCTION

There has been increasing interest in large-scale clustering measurements of active galactic nucleus (AGNs) in recent years. Such measurements (see review by Krumpe et al. 2014) not only allow one to study the distribution of matter in the Universe out to redshifts where it becomes very challenging and observationally expensive to detect galaxies in large numbers, but they also can be used to constrain theoretical models of AGN/galaxy coevolution, feedback mechanisms, AGN host-galaxy properties, the distribution of AGNs with dark matter halo (DMH) mass, and the fueling process(es) of supermassive black holes (SMBH) (e.g., Porciani et al. 2004; Gilli et al. 2005, 2009; Yang et al. 2006; Coil et al. 2009; Ross et al. 2009; Cappelluti et al. 2010; Krumpe et al. 2010a, 2012; Allevalo et al. 2011; Miyaji et al. 2011; Mountrichas & Georgakakis 2012; Koutoulidis et al. 2013).

Spatial correlation measurements with several tens

of thousands of galaxies yield significant clustering dependences on galaxy properties such as luminosity, morphological type, spectral type, and redshift (e.g., Norberg et al. 2002; Madgwick et al. 2003; Zehavi et al. 2005b, 2011; Meneux et al. 2006, 2009; Coil et al. 2008). These findings confirm the hierarchical model of structure formation in which more massive, and hence more luminous, galaxies reside in more massive DMHs and are therefore clustered more strongly (e.g., Zehavi et al. 2005b, 2011; Coil et al. 2006). Whether this relation should also apply to AGN luminosity is not trivial. Since the AGN luminosity depends primarily on the mass of the SMBH (M_{BH}), the accretion rate relative to Eddington (L/L_{EDD}), and the radiative accretion efficiency, a relation between clustering and AGN luminosity should ultimately be due to a connection between DMH mass and one or more of these physical parameters.

Based on smoothed-particle hydrodynamic simulations using GADGET (Springel 2005), Booth & Schaye (2010) explore the correlation between SMBH mass and the mass of the hosting DMH. In the simulations, the black holes grow either by the accretion of ambient gas or mergers. The black holes also inject a fixed fraction of the rest mass energy of the gas into the surrounding medium. A self-regulating black hole injects enough energy to displace gas from the host galaxy on longer timescales. The binding energy of the gas is determined by the DMH potential. Thus, Booth & Schaye (2010) conclude that the mass of the SMBH is regulated primarily by the DMH mass and not the stellar mass of the galaxy. Fanidakis et al. (2012) use the semianalytical galaxy-formation model GALFORM (Cole et al. 2000; more details on their simulations are given below in

mkrumpe@aip.de

¹ Leibniz-Institut für Astrophysik Potsdam (AIP), An der Sternwarte 16, D-14482 Potsdam, Germany

² European Southern Observatory, ESO Headquarters, Karl-Schwarzschild-Straße 2, D-85748 Garching bei München, Germany

³ University of California, San Diego, Center for Astrophysics and Space Sciences, 9500 Gilman Drive, La Jolla, CA 92093-0424, USA

⁴ Max-Planck-Institut für extraterrestrische Physik, Gießenbachstraße 1, D-85748 Garching, Germany

⁵ IAUNAM-E (Instituto de Astronomía de la Universidad Nacional Autónoma de México, Ensenada), P.O. Box 439027, San Diego, CA 92143-9027, USA

⁶ Max-Planck-Institut für Astronomie, Königstuhl 17, 69117 Heidelberg, Germany

Sect. 6.4) and find a correlation between SMBH mass and DMH mass at almost all cosmic times ($z = 0.0 - 6.2$). Volonteri et al. (2011) use the measured black hole mass, velocity dispersion σ , and asymptotic circular velocity of 25 local galaxies from Kormendy et al. (2011) to show that, although with some scatter, the black hole masses correlate well with the parent DMH masses.

AGN clustering studies can be used to observationally test such predictions. Several studies have measured the large-scale clustering dependence on AGN on properties such as X-ray luminosity, with varying results. Coil et al. (2009) find no correlation between the AGN X-ray luminosity and the clustering strength at $z = 0.7 - 1.4$. At $z \sim 0.1$, Mountrichas & Georgakakis (2012) also detect no significant correlation in their sample of *XMM-Newton*-selected AGNs. Yang et al. (2006) reports a tentative ($\sim 1\sigma$) dependence of the clustering signal, such that the brighter sample is more clustered than the fainter sample. Cappelluti et al. (2010) and Koutoulidis et al. (2013) verify this finding using different AGN samples at different redshifts. Koutoulidis et al. (2013) use a large sample of ~ 1500 AGNs from the Chandra Deep Field (CDF) North and South, the extended CDF South, COSMOS, and AEGIS. The median redshifts of their low and high L_X AGN samples are $\langle z \rangle \sim 0.8 - 1.1$. Except for the CDF South survey, they find weak X-ray luminosity dependences at a level of up to $\sim 2\sigma$.

One way to reduce the uncertainties involved in clustering measurements — beyond using larger AGN samples — is to compute the cross-correlation function (CCF) with a dense galaxy sample instead of computing the autocorrelation function (ACF) of the AGNs. Several studies (e.g., Li et al. 2006; Coil et al. 2007, 2009; Wake et al. 2008; Hickox et al. 2009; Mountrichas et al. 2013; Georgakakis et al. 2014) demonstrate the potential of this approach and compute the CCF between AGNs and a large sample of galaxies to infer the ACF of the AGNs. The significant increase in the number of pairs at a given separation, used to measure the clustering strength, reduces the uncertainties in the spatial correlation function compared to the direct measurements of the AGN ACF.

In Krumpe et al. (2010a, hereafter Paper I), we use the same technique as Coil et al. (2009) to measure the CCF between *ROSAT* All-Sky Survey (RASS) AGNs identified in the Sloan Digital Sky Survey (SDSS) and a large set of SDSS luminous red galaxies (LRGs) at $0.16 < z < 0.36$. The study is based on SDSS data release 4+ (DR4+). The unprecedented low uncertainties of the inferred broad-line AGN ACF allow us to split the sample into low and high X-ray luminosity subsamples and to report a $\sim 2.5\sigma$ X-ray luminosity dependence of broad-line AGN clustering. We find that higher luminosity AGNs cluster more strongly than their lower luminosity counterparts. Consequently, higher luminosity X-ray AGNs reside, on average, in more massive DMHs than do lower luminosity X-ray AGN.

In the second paper of this series (Miyaji et al. 2011, hereafter Paper II), we describe a novel method of applying the halo occupation distribution (HOD) modeling technique directly to the precise measured CCF between RASS/SDSS AGNs and SDSS LRGs to constrain the distribution of AGNs as a function of DMH mass. This method also allows us to derive the large-scale bias pa-

rameter of the AGN sample with much lower systematic uncertainties than using a phenomenological power-law fit, as is often done. As shown in Paper II, the X-ray luminosity dependence is more prominent in the one-halo term ($r_p < 1 h^{-1}$ Mpc). The HOD-based typical DMH masses derived from the two-halo term for the high- and low-luminosity RASS/SDSS AGN subsamples differ by $\sim 1.8\sigma$. In addition, we find that models where the AGN fraction among satellites decreases with DMH mass beyond $M_{\text{DMH}} \sim 10^{12} h^{-1} M_\odot$ are preferred. This is in contrast to what is found for satellite galaxies without AGNs (Zheng et al. 2009; Zehavi et al. 2011).

In the third paper (Krumpe et al. 2012, hereafter Paper III), we extend the cross-correlation measurements to lower and higher redshifts, covering a redshift range of $z = 0.07 - 0.50$. We show that the weak X-ray luminosity dependence of broad-line AGN clustering is also found if radio-detected AGNs are excluded. Furthermore, we compute the large-scale clustering for optically selected broad-line SDSS AGNs using the final SDSS DR7, but we detect no optical luminosity dependence on the clustering strength, although the optical broad-line SDSS AGN sample in $0.16 < z < 0.36$ contains more than twice as many objects as the RASS/SDSS AGN sample. We conclude that the most likely explanation for this result is the smaller dynamic range probed in optical luminosities compared to X-ray luminosities.

In this paper we focus on the redshift range $0.16 < z < 0.36$, where the CCF of RASS/SDSS AGNs and LRGs has the highest signal-to-noise ratio (S/N). We fit the $H\alpha$ line profile in the SDSS spectra of broad-line AGN to infer the M_{BH} and the L/L_{EDD} . Dividing the AGN sample into low and high M_{BH} mass, as well as low and high L/L_{EDD} , provides insights into the main physical driver of the weak detected X-ray luminosity dependence of broad-line AGN clustering.

This paper is organized as follows. In Section 2, we describe the properties of the LRG tracer set and the AGN samples. Section 3 provides details on how we fit the $H\alpha$ line profile in the optical SDSS AGN spectra, derive the M_{BH} , estimate L/L_{EDD} , and define our AGN subsamples. In Section 4, we briefly summarize the cross-correlation technique, how the AGN ACF is inferred from this, and how we derive the large-scale bias parameters using HOD modeling. Section 5 provides the results of our clustering measurements. The detailed results of the HOD modeling of the CCFs presented in this paper and in paper III will be included in a future paper (T. Miyaji et al. in preparation). Our results are discussed in Section 6, and we present our conclusions in Section 7. Throughout the paper, all distances are measured in comoving coordinates and given in units of h^{-1} Mpc, where $h = H_0/100 \text{ km s}^{-1} \text{ Mpc}^{-1}$, unless otherwise stated. We use a cosmology of $\Omega_m = 0.3$, $\Omega_\Lambda = 0.7$, and $\sigma_8(z=0) = 0.8$, which is consistent with the *WMAP* data release 7 (Table 3 of Larson et al. 2011). The same cosmology is used in Papers I–III. Luminosities and absolute magnitudes are calculated for $h = 0.7$. We use AB magnitudes throughout the paper. All uncertainties represent 1σ (68.3%) confidence intervals unless otherwise stated.

The data sets used in this study are drawn from the SDSS, which consists of an imaging survey in five bands and an extensive spectroscopic follow-up survey with a fiber spectrograph. The selection of the optically selected AGN candidates is described in Richards et al. (2002). LRGs are chosen by following Eisenstein et al. (2001).

2.1. SDSS Luminous Red Galaxy Sample

The selection of SDSS LRGs follows the procedure described in Section 2.1 of Paper I and Section 2.2 of Paper III. Here we briefly summarize the sample selection. We extract LRGs from the web-based SDSS Catalog Archive Server Jobs System⁷ using the flag “galaxy_red,” which is based on the selection criteria defined in Eisenstein et al. (2001). We verify that the extracted objects meet all LRG selection criteria and create a volume-limited sample with $0.16 < z < 0.36$ and $-23.2 < M_g^{0.3} < -21.2$, where $M_g^{0.3}$ is based on the extinction-corrected r_{petro}^* magnitude, k -corrected and passively evolved to rest-frame g_{petro}^* magnitudes at $z = 0.3$. We consider only LRGs that fall into the SDSS area with a DR7 spectroscopic completeness ratio of greater than 0.8 and that have a redshift confidence level of greater than 0.95. The SDSS geometry and completeness ratio are expressed in terms of spherical polygons (Hamilton & Tegmark 2004). The file is publicly available^{8,9} through the New York University Value-Added Galaxy Catalog (NYU-VAGC) website (Blanton et al. 2005).

We correct for the SDSS fiber collision as described in detail in Krumpe et al. (2010a, 2012). We have to assign to approximately 2% of all LRGs in our sample a redshift due to the fiber collision problem.

The construction of the random LRG sample is identical to the procedure described in Section 3.1 of Paper I. Our LRG random sample contains 200 times as many objects as the real LRG sample. We generate a set of random R.A. and decl. values within DR7 areas with spectroscopic completeness ratios of greater than 0.8, populate areas with higher completeness ratios more than ones with lower completeness ratios, and randomly assign redshifts to the objects in the sample by using the smoothed redshift profile of the observed redshift distribution.

2.2. RASS/SDSS AGN Samples

The *ROSAT* All-Sky Survey (RASS, Voges et al. 1999) is currently still the most sensitive all-sky survey in the soft (0.1–2.4 keV) X-ray regime. Anderson et al. (2003, 2007) positionally cross-correlate RASS sources with SDSS spectroscopic objects and classify RASS- and SDSS-detected AGNs based on SDSS DR5. They find 6224 AGN with broad permitted emission lines in excess of 1000 km s^{-1} FWHM and 515 narrow permitted emission line AGNs matching RASS sources within 1 arcmin. More details on the sample selection are given in Section 2.2 of Paper I and Anderson et al. (2003, 2007). Since *ROSAT* observed the sky in the soft energy band (0.1–2.4 keV), the RASS/SDSS AGN sample is biased toward AGNs with little to no X-ray absorption. The vast

majority of the optical counterparts are therefore AGNs with broad emission lines and UV excess. There is no overlap between the RASS/SDSS AGNs and the LRG sample.

To study the X-ray luminosity dependence of the clustering of these AGNs, we have to limit the SDSS footprint to the publicly available DR4+ geometry. We split our sample in the redshift range $0.16 < z < 0.36$ into subsamples according to X-ray luminosity. We use a 0.1–2.4 keV observed luminosity cut (assuming a photon index $\Gamma = 2.5$, corrected for Galactic absorption) of $\log(L_X/[\text{erg s}^{-1}]) = 44.29$. The observed flux in the 0.1–2.4 keV band has a large soft-excess contribution that is not representative of the underlying intrinsic, hard power-law X-ray spectrum. Thus, we use the template *XMM-Newton* spectrum of powerful radio-quiet *ROSAT* QSOs from Krumpe et al. (2010b) to estimate the corresponding flux in the 0.5–10 keV and 2–10 keV energy ranges. Using the median redshift of the sample ($z = 0.27$), the cut at 0.1–2.4 keV corresponds to a cut at $\log(L_{0.5-10 \text{ keV}}/[\text{erg s}^{-1}]) = 43.7$ and $\log(L_{2-10 \text{ keV}}/[\text{erg s}^{-1}]) = 43.4$.

As an alternative estimate, we match our RASS AGN sample with the 3XMM-DR5 catalog (Rosen et al. 2015). We fit a regression line between the RASS 0.1–2.4 keV fluxes and the *XMM-Newton* 2–12 keV fluxes. Using *Xspec* (Arnaud et al. 1996), we model the same ratio with a broken power law and determine the luminosity ratios in the ranges 0.1–2.4 keV, 0.5–10 keV, and 2–10 keV. We find somewhat smaller corrections: $\log(L_X/[\text{erg s}^{-1}]) = 44.29$ corresponds to $\log(L_{0.5-10 \text{ keV}}/[\text{erg s}^{-1}]) = 43.9$ and $\log(L_{2-10 \text{ keV}}/[\text{erg s}^{-1}]) = 43.7$. This approach has the disadvantage that the observations were taken over a decade apart, and temporal variation in the X-ray luminosity/flux of the objects will affect the estimate. However, one could argue that such variations are effectively averaged over in a large sample of X-ray objects as used here. Fits to the 0.5–10 keV *XMM-Newton* spectra verified that the vast majority ($\sim 95\%$) of the cross-matched RASS/XMM AGNs are unabsorbed in the X-rays ($N_{\text{H}} < 10^{21} \text{ cm}^{-2}$), while the remaining sources show absorption at a level of only a few 10^{21} cm^{-2} .

We calculate the comoving number densities as described in detail in Paper I. For a given R.A. and decl., we compute the limiting observable RASS count rate and infer the absorption-corrected flux limit versus survey area for RASS/SDSS AGNs. We then compute the comoving volume available to each object (V_a) to be included in the sample (Avni & Bahcall 1980). The comoving number density follows by computing the sum of the available volume over each object, $n_{\text{AGN}} = \sum_i 1/V_{a,i}$. The comoving number densities for the total, high L_X , and low L_X subsamples are 6.0, 0.12, and $5.8 \times 10^{-5} h^3 \text{ Mpc}^{-3}$, respectively.

3. DERIVING M_{BH} AND L/L_{EDD} THROUGH $\text{H}\alpha$ LINE PROFILE FITS

The so-called virial method is routinely employed to estimate M_{BH} from single-epoch spectra based solely on the width of broad emission lines together with an appropriate continuum luminosity (Kaspi et al. 2000; Peterson & Wandel 2000; Vestergaard 2002). The FWHM of $\text{H}\beta$ (FWHM $_{\text{H}\beta}$) and the rest-frame contin-

⁷ <http://casjobs.sdss.org/CasJobs/>

⁸ <http://sdss.physics.nyu.edu/lss/dr72>

⁹ <http://sdss.physics.nyu.edu/lss/dr4plus>

uum luminosity at 5100 \AA (L_{5100}) are most commonly used to compute M_{BH} for low-redshift AGNs, because the corresponding calibrations are the best-studied ones to date. On the other hand, the $\text{H}\alpha$ line offers a higher S/N than $\text{H}\beta$ and tight relations between $\text{FWHM}_{\text{H}\beta}$ and $\text{FWHM}_{\text{H}\alpha}$, as well as between L_{5100} and $L_{\text{H}\alpha}$, have been established (Greene & Ho 2005, Schulze et al. 2010). Consequently, accurate M_{BH} estimates can also be obtained from the broad $\text{H}\alpha$ line.

The simultaneous use of the broad $\text{H}\alpha$ line as a proxy for the velocity dispersion in the broad-line region (BLR) and for the AGN luminosity has two major advantages. First, we avoid any potential contamination of L_{5100} by host galaxy light and the influence of the broad Fe II emission in type I AGNs on the broad $\text{H}\beta$ FWHM measurement (Greene & Ho 2005). Second, we obtain reliable BH mass estimates even for those objects where the S/N of $\text{H}\beta$ would be too low.

3.1. Fitting the $\text{H}\alpha$ Line Profile

We retrieve the individual SDSS DR7 optical spectra for our entire RASS/SDSS AGN sample in order to measure the luminosity and FWHM of $\text{H}\alpha$ for each AGN. Although the FWHM and integrated flux of $\text{H}\alpha$ could in principle be measured directly from the spectra, the narrow $\text{H}\alpha$ and $[\text{N II}]$ lines on top of the broad $\text{H}\alpha$ line have a significant impact on the estimated M_{BH} and L/L_{EDD} values (Fig. 1, left panels), as highlighted by Denney et al. (2009). The narrow $\text{H}\alpha$ originates from star formation in the host galaxy and the narrow-line region (NLR) photoionized by the AGN outside of the central. Deblending the broad and narrow emission lines is therefore essential to minimize systematic effects by separating the contribution from the BLR and the NLR/host in the $\text{H}\alpha$ line.

One major complication in modeling the AGN spectra is the commonly complex, non-Gaussian shape of the broad $\text{H}\alpha$ line. Previous studies have used multiple Gaussian components (e.g., Brotherton et al. 1994; Sulentic et al. 2002; Shen et al. 2008; Schulze et al. 2009) or high-order Gauss-Hermite polynomials (e.g., Salviander et al. 2007; McGill et al. 2008; Stern & Laor 2012) to describe the asymmetries of the line. We test both approaches to fit the SDSS spectra and conclude that the latter is more robust against the choice of initial parameter estimates.

We simultaneously model the broad $\text{H}\beta$ and $\text{H}\alpha$ lines together with the narrow $\text{H}\beta$, $[\text{O III}] \lambda 4960, \lambda 5007$, $\text{H}\alpha$, and $[\text{N II}] \lambda 6548, \lambda 6583$ emission lines. We briefly describe our algorithm of modeling the broad $\text{H}\alpha$ line below and follow an approach similar to Stern & Laor (2012). The model of the $\text{H}\beta$ region (left panels in Fig. 1) is only used to better constrain the parameters of narrow lines. The well-isolated narrow $[\text{O III}]$ line in the $\text{H}\beta$ region gives parameter restrictions that are superior to the narrow-line profiles in the $\text{H}\alpha$ region, where the narrow and broad lines can be strongly blended.

As a first step, the approximate underlying continua are independently subtracted from the $\text{H}\beta$ and $\text{H}\alpha$ lines by linear interpolation between the adjacent rest-frame spectral regions $4720\text{--}4760 \text{ \AA}$ and $5070\text{--}5130 \text{ \AA}$, as well as $6150\text{--}6230 \text{ \AA}$ and $6750\text{--}6950 \text{ \AA}$, respectively. The fit requires initial guesses for the broad and narrow line

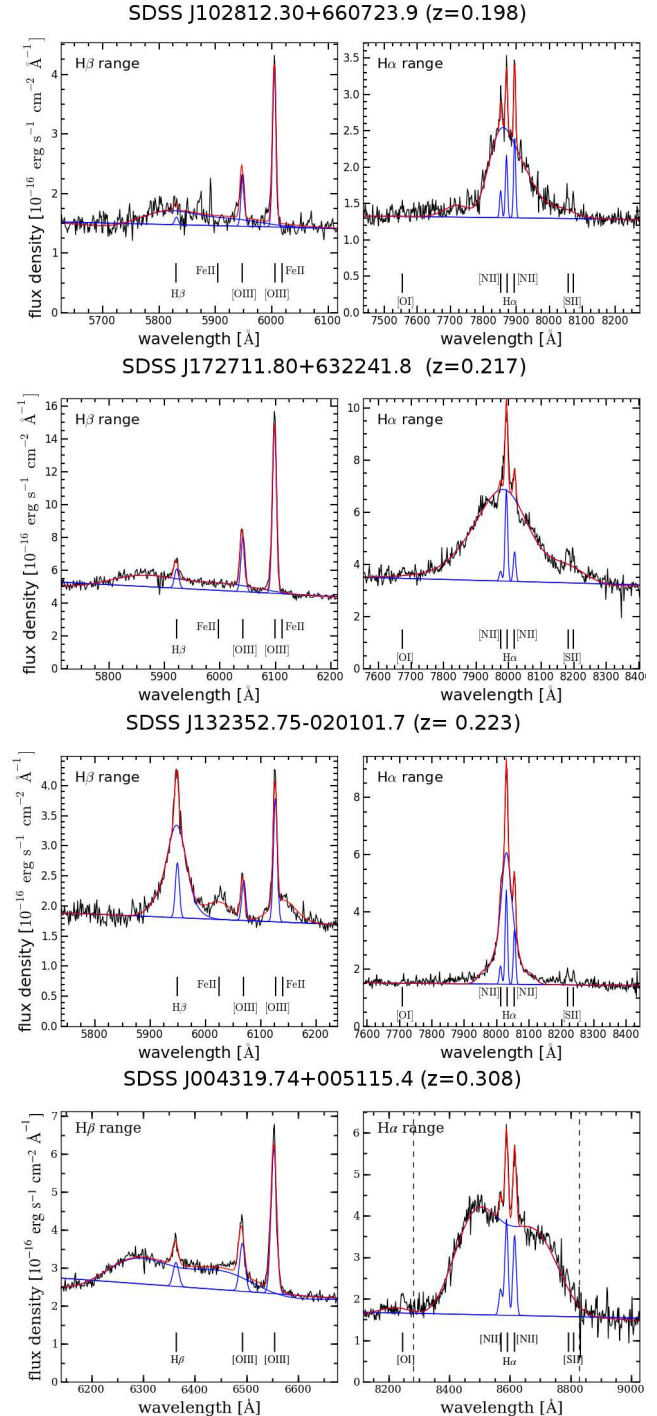


FIG. 1.— Observed SDSS spectra (black solid lines) and the corresponding models (red solid lines) in the observed $\text{H}\beta$ (left panels) and $\text{H}\alpha$ (right panels) wavelength ranges. The fitted individual line components are indicated by blue solid lines (underlying continuum, narrow and broad lines). The most prominent line features are labeled.

components. The initial guesses for the FWHM and line flux of the broad lines are determined by a fourth-order Gauss-Hermite polynomial of the entire $\text{H}\alpha$ line and assuming standard $\text{H}\alpha$ and $\text{H}\beta$ ratios. The initial guesses of the narrow line components are based on the total flux of the observed $[\text{O III}]$ line and typical narrow-line AGN ratios. An eighth-order Gauss-Hermite poly-

nomial provides a good fit for the full model of complex broad $H\beta$ and $H\alpha$ line shapes in almost all cases. All narrow emission lines are assumed to have ordinary Gaussian profiles that are coupled in redshift, velocity dispersion, and line ratios for doublets. While $[O\ III]$ can exhibit a blueshifted wing in cases with an outflow (e.g., Mullaney et al. 2013), the narrow component usually strongly dominates the line flux, and therefore a single-component line fit is generally robust when coupled to lower ionization lines like $[N\ II]$. In cases where the outflow component dominates, we decouple $[O\ III]$ from the fit to other narrow lines, as described below. We also add the two dominant $Fe\ II$ lines in the $H\beta$ wavelength range as Gaussians to our model. The best-fit model is determined by using a Levenberg–Marquardt minimization algorithm, where spectral regions of unconsidered weak narrow emission lines, e.g., $[O\ I]\lambda 6300$ and $[S\ II]\lambda 6718, \lambda 6732$, have been masked out along with pixels assigned as bad by the SDSS spectroscopic pipeline.

We deviate slightly from the scheme above in the following three cases: (1) the broad $H\beta$ line is too weak to be modeled, (2) the $[O\ III]$ line exceeds a width of 600 km sec^{-1} , or (3) the narrow $H\alpha$ line flux is negative in the initial best-fit model. In the first case, we repeat the model without any broad $H\beta$ and $Fe\ II$ components. In the second and third case, the $[O\ III]$ line is likely to be affected by outflows and may not match the line profile of the other narrow lines. Therefore, we allow the $[O\ III]$ line to have an independent redshift and velocity dispersion with respect to the other narrow lines.

One percent of the RASS/SDSS spectra do not allow such an analysis because significant parts of the spectral range around $H\alpha$ or $[O\ III]$ are masked out. We do not expect any significant impact on our study, due to the low number of objects for which this is the case (see also Sect. 5.1 below).

Examples of the best-fit models for typical S/N AGN spectra are shown in Figure 1. From those best-fit models we measure the FWHM and integrated flux of the broad-line $H\alpha$ component, as these are the parameters required to estimate M_{BH} and L/L_{EDD} . Our model is not designed to provide a perfect fit to $H\alpha$ line profiles for the most complex cases. However, the model deviations concerning the $H\alpha$ width and flux are much smaller than the systematics of virial M_{BH} estimates (see discussion in Denney et al. 2009). To assess the uncertainties of the derived parameters and to identify unreliable models, we generate 100 realizations of the same spectrum by replacing each pixel within its 1σ variance given by the SDSS error spectrum and analyze the artificial spectra in the same manner. The uncertainty for each quantity is then taken as the dispersion (1σ error corresponding to 68.3%) in the best-fit value of all 100 measurements.

We compared our measurements with those of Stern & Laor (2012) to cross-check our results with a completely independent algorithm (Fig. 2) and to provide an estimate of the systematic uncertainties. In contrast to our study, their sample contains lower luminosity AGNs at a slightly different redshift range. Thus, the samples only overlap partially. For the broad $H\alpha$ FWHM and luminosity, we find relatively tight correlations around the unity relation. The measurements of the broad $H\alpha$ FWHM exhibit a larger scatter and are

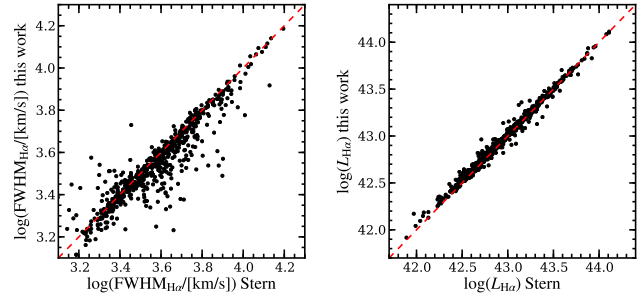


FIG. 2.— Comparison of the fitted FWHM and luminosity of the broad $H\alpha$ line component between our work and Stern & Laor (2012), for sources in both studies. The dashed red lines show the unity correlations. The 1σ scatter about these lines is 0.08 dex (left) and 0.04 dex (right), respectively.

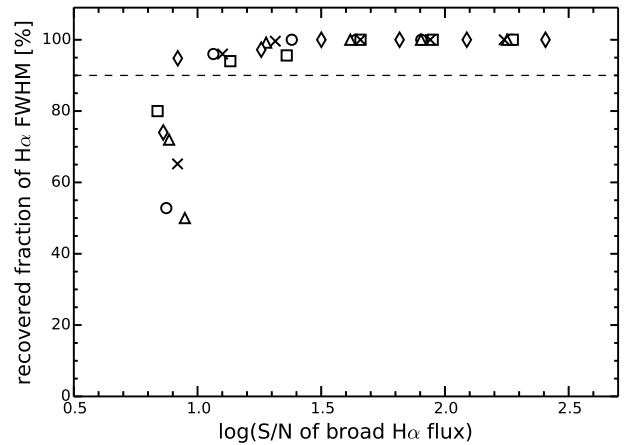


FIG. 3.— Accuracy in recovering the FWHM value of the broad $H\alpha$ line as a function of the signal-to-noise ratio (S/N) of the integrated flux of the broad $H\alpha$ line. We use high S/N spectra to simulate 250 realizations at various degraded S/N levels. Within each S/N bin, we determine the fraction of spectra for which the FWHM is within 40% of the original high S/N spectrum (see text for details). We show the results for five different objects indicated by different symbols.

slightly skewed toward lower values using our method. We inspected those spectra and identify a common characteristic in these cases: the narrow lines are broader and weaker than for the other AGNs in the sample. Thus, deblending the narrow $[NII]+H\alpha$ from the broad $H\alpha$ line can be challenging. This is particularly true for broad $H\alpha$ lines with a FWHM less than 4000 km s^{-1} . In summary, our line-profile fitting method provides robust estimates for the FWHM and line flux within their systematic uncertainties and without the need for human interaction.

3.2. Estimating M_{BH}

The virial black hole mass is estimated by combining the empirically calibrated BLR size-luminosity relation, derived from reverberation mapping monitoring of nearby AGNs, and assuming virialized BLR motions, $M_{BH} = f_{vir} v^2 R_{BLR} G^{-1}$, where v is the FWHM of broad lines in the AGN spectrum and f_{vir} is the virial factor representing the BLR kinematics. Several different estimators for M_{BH} have independently been reported in the literature using different BLR size-luminosity relations and virial factors based on different assumptions. Here we employ two different calibrations to check their potential impact on our results. The first is from

McLure & Dunlop (2004):

$$\frac{M_{\text{BH}}}{M_{\odot}} = 4.7 \left(\frac{L_{5100}}{10^{44} \text{erg s}^{-1}} \right)^{0.61} \left(\frac{\text{FWHM}_{\text{H}\beta}}{\text{km s}^{-1}} \right)^2 \quad (1)$$

which is also used by Shen et al. (2009) to estimate M_{BH} for all unobscured, optically selected SDSS AGN. The second calibration is based on the most recent BLR size-luminosity relation of Bentz et al. (2009), assuming a virial factor of $f_{\text{vir}} = 5.5$, which is empirically determined by Onken et al. (2004):

$$\frac{M_{\text{BH}}}{M_{\odot}} = 8.13 \left(\frac{L_{5100}}{10^{44} \text{erg s}^{-1}} \right)^{0.52} \left(\frac{\text{FWHM}_{\text{H}\beta}}{\text{km s}^{-1}} \right)^2. \quad (2)$$

Throughout the paper, we use the second calibration (Bentz et al. 2009) for the estimates of the black hole masses. In Sect. 5.1 below we test the robustness of our clustering results if the first calibration method is used instead. As we demonstrate below, we find very similar results using either calibration.

In order to use our measurements from the $\text{H}\alpha$ line to estimate M_{BH} , we have to replace L_{5100} by $L_{\text{H}\alpha}$ and $\text{FWHM}_{\text{H}\beta}$ by $\text{FWHM}_{\text{H}\alpha}$ in Equations (1) and (2), following Greene & Ho (2005) (their Equations 1 and 3).

Denney et al. (2009) point out that the inclusion of low S/N spectra adds a systematic offset in M_{BH} estimates because the line width is systematically underestimated. Therefore, we enforce a lower cutoff in the measured S/N level of the broad $\text{H}\alpha$ line flux. We determine the cutoff S/N by selecting the five AGN spectra with the highest S/N. Then, we artificially degrade the S/N gradually down to a continuum S/N of 1. For each S/N level, we generate 250 spectra and model these individual spectra with our line-profile fitting method.

At an $\text{H}\alpha$ FWHM uncertainty level of greater than 40%, the measurement uncertainties exceed the commonly assumed systematic uncertainties for virial M_{BH} estimates of ~ 0.3 dex. More than 90% of all of our generated spectra have FWHM uncertainties of less than 40% if we restrict the $\text{H}\alpha$ S/N to values greater than 10 (Figure 3). Consequently, we adapt this S/N threshold as a limit for selecting objects that yield reliable M_{BH} estimates. This cutoff leads to a removal of 189 out of 1538 objects (12% of the sample). We apply this S/N cut and compare our measured FWHM values to the ones from Stern & Laor (2012). The observed scatter in FWHM between both methods is 0.08 dex, which corresponds to an M_{BH} error of 0.16. This can be interpreted as a simple estimate of the minimum systematic uncertainty in the M_{BH} determination, which is reflected in the commonly assumed total ~ 0.3 dex systematic uncertainty of this method.

The main purpose of this paper is to study the clustering of AGN samples with low and high M_{BH} and L/L_{EDD} , respectively. Any uncertainty in the calibration of M_{BH} will affect our entire sample similarly. Thus, our results will not depend on the absolute accuracy of the M_{BH} calibration because we are interested only in relative M_{BH} values such that we can divide the full sample into low and high M_{BH} subsamples.

3.3. Estimating L/L_{EDD}

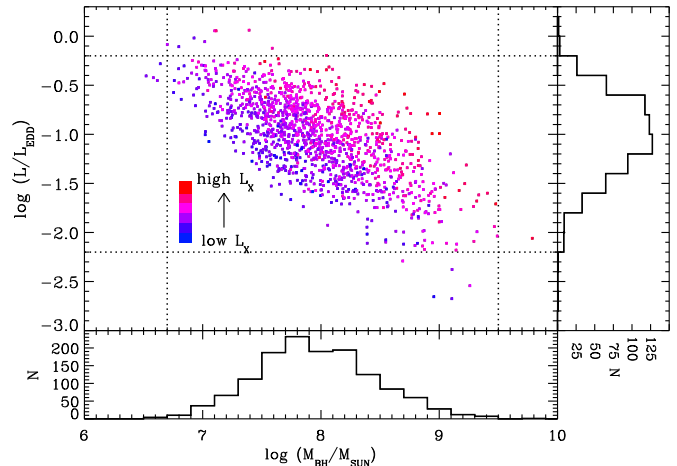


FIG. 4.— M_{BH} vs. L/L_{EDD} for luminous, unabsorbed, broad-line, X-ray selected RASS/SDSS AGNs with a broad $\text{H}\alpha$ luminosity of $S/N > 10$. The color of the symbols encodes the X-ray luminosity of the sources. The lower and right panels show histograms of M_{BH} and L/L_{EDD} , respectively, for the full sample. The dotted lines mark the restriction of the parameter space in our analysis to remove extreme objects.

The Eddington ratio L/L_{EDD} is the ratio between the bolometric and the Eddington luminosity ($L_{\text{edd}} = 1.26 \times 10^{38} M_{\text{BH}}/M_{\odot} \text{ erg s}^{-1}$). The quantity is commonly derived by using the inferred M_{BH} and the optical continuum luminosity at 5100 \AA , adopting a certain bolometric correction factor. Different bolometric correction factors used to estimate the bolometric luminosity L_{bol} from L_{5100} are quoted in the literature (Kaspi et al. 2000; McLure & Dunlop 2004; Richards et al. 2006a). While these correction factors are subject to uncertainties, they are required to estimate the bolometric luminosity if only a single-epoch optical spectrum is available. We use a correction factor of $f = 10.3$ (Richards et al. 2006a), which is consistent with values used by other studies. Again, we use the relation from Greene & Ho (2005) to estimate L_{5100} from $L_{\text{H}\alpha}$ for the computation of L_{bol} .

3.4. Defining X-ray Selected AGN Subsamples

The RASS/SDSS AGNs in our sample do not uniformly populate the $M_{\text{BH}} - L/L_{\text{EDD}}$ plane (Figure 4). Although there is substantial scatter, on average, higher L/L_{EDD} are found in AGNs with lower M_{BH} . While the absence of objects in the upper right corner of this plane is not an observational bias, but reflects the nonexistence of (unabsorbed) RASS/SDSS AGNs with both high M_{BH} and high L/L_{EDD} in the redshift range studied here, the lack of objects in the lower left corner reflects an observational bias. AGNs with low L/L_{EDD} and low M_{BH} are too weak to produce a significant broad $\text{H}\alpha$ line relative to the host galaxy continuum. The $\text{H}\alpha$ flux S/N cutoff used here primarily removes objects with $\log(M_{\text{BH}}/M_{\odot}) \sim 7-8$.

Since M_{BH} and L/L_{EDD} are correlated in our full sample, and we aim to reveal which of these quantities drives the observed X-ray luminosity dependence of AGN clustering, doing a simple cut of the full sample into low and high M_{BH} subsamples, as well as high and low L/L_{EDD} subsamples, will not be useful. When creating subsamples that depend on one parameter, the distribution of the second parameter in both subsamples must be the same. This “matching” of the subsamples is a commonly

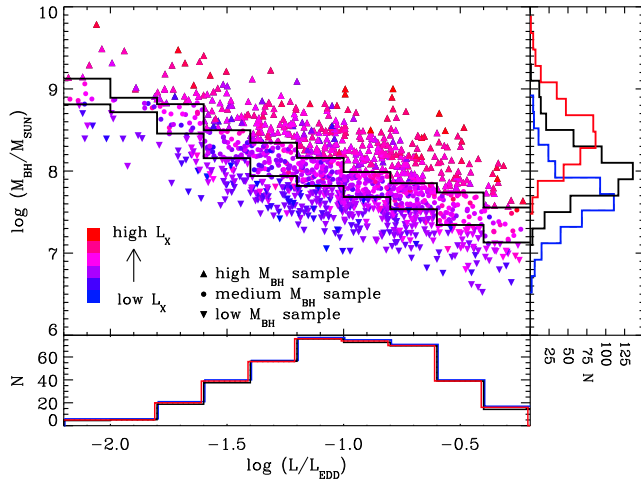


FIG. 5.— Low (filled down-pointing triangles), medium (filled circles), and high (filled up-pointing triangles) M_{BH} RASS/SDSS AGN subsamples with matched L/L_{EDD} distributions. The top panel shows the $L/L_{\text{EDD}}-M_{\text{BH}}$ plane. The color of the points encodes the X-ray luminosity from lowest L_X (blue) to highest L_X (red). The solid lines are for visual guidance and mark the division of the full AGN sample into low, medium, and high M_{BH} subsamples. The bottom and right panels show the L/L_{EDD} and M_{BH} histograms of the low (blue), medium (black), and high (red) M_{BH} subsamples, respectively. Since the medium M_{BH} subsample contains more objects than the low and high subsamples, we normalized the total number of this sample in the L/L_{EDD} histogram to match the other samples. For clarity, we slightly shift the x values of the low and high M_{BH} subsamples in the histograms.

used method in clustering measurements (e.g., Coil et al. 2009). However, one has to test that the procedure of creating matched subsamples is not introducing a bias to the clustering results. We will do so below by testing different methods to produce matched subsamples (see Sect. 5.1).

Before creating low and high M_{BH} subsamples, objects that lie outside the range $-2.2 < \log(L/L_{\text{EDD}}) < -0.2$ are removed. We then determine the number of objects in each L/L_{EDD} bin, using a bin width of 0.2 (logarithmic scale). In each L/L_{EDD} bin, we create three subsamples: 30% of objects with the lowest M_{BH} , 40% with medium M_{BH} , and 30% of objects with the highest M_{BH} (Figure 5). The procedure creates low, medium, and high M_{BH} AGN subsamples with extremely similar (“matched”) L/L_{EDD} distributions but different median M_{BH} (see Table 1). All M_{BH} AGN subsamples have median $\langle \log(L/L_{\text{EDD}}) \rangle = -1.00$.

The low (30%), medium (40%), and high (30%) L/L_{EDD} RASS/SDSS AGN subsamples with matched M_{BH} distributions are created by first applying a cut of $6.7 < \log(M_{\text{BH}}/M_{\odot}) < 9.5$ to remove extreme sources and then following the same approach as described above, using bins of M_{BH} with a bin width of 0.2 (logarithmic scale). All L/L_{EDD} AGN subsamples have median $\langle \log(M_{\text{BH}}/M_{\odot}) \rangle = 7.92 - 7.93$.

Figures 4 and 5 show that divisions into low, medium, and high M_{BH} as well as L/L_{EDD} are very similar to divisions into low, medium, and high L_X . Thus, one cannot anticipate if the X-ray luminosity clustering dependence is related to L/L_{EDD} or M_{BH} , as we aim to test here.

The directly observed parameters FWHM and $L_{\text{H}\alpha}$ do not correlate with each other as strongly as M_{BH} and L/L_{EDD} (see Fig. 6). However, we decide to use the same method to create subsamples defined by FWHM

and $L_{\text{H}\alpha}$ as well. Thus, we again split the full sample into three subsamples defined using one parameter, while maintaining the same distribution in the other parameter of interest. To create subsamples in FWHM, we first limit to objects with $41.7 < \log(L_{\text{H}\alpha}/[\text{erg s}^{-1}]) < 44.1$ and then use a bin width of 0.2. All FWHM AGN subsamples have $\langle \log(L_{\text{H}\alpha}/[\text{erg s}^{-1}]) \rangle = 42.72 - 42.73$. To create subsamples in $L_{\text{H}\alpha}$, we first limit to objects with $2.9 < \log(\text{FWHM}/[\text{km s}^{-1}]) < 4.1$, and then use bins of width 0.1, using the logarithmic values of FWHM. This choice of bin width ensures a similar numbers of bins as compared to the subsamples defined in $L_{\text{H}\alpha}$. The median FWHM of all $L_{\text{H}\alpha}$ subsamples is $\langle \text{FWHM} \rangle = 2850 - 2960 \text{ km s}^{-1}$.

As we have to exclude $\sim 13\%$ of the RASS/SDSS AGN sample studied in Papers I–III to fulfill our S/N requirement of the broad $\text{H}\alpha$ line flux for reliable M_{BH} estimates, we create low and high X-ray luminosity subsamples of the reduced AGN sample used here. We use a simple 0.1–2.4 keV luminosity cut (with no matching of the distribution of another parameter) of $\log(L_X/[\text{erg s}^{-1}]) = 44.29$, identical to that used in Papers I–III.

We also apply simple M_i cuts at $M_i = -22.10$ mag and $M_i = -22.70$ mag to divide the X-ray-selected AGN sample into a faint (33% of all objects), medium (34%), and luminous (33%) M_i subsamples. Finally, we compute from the SDSS optical spectra the rest-frame absolute magnitude in the band between 5500 and 6800 Å, which includes the $\text{H}\alpha$ line for all objects. We do this as the X-ray and optically selected sample covers a redshift range of $0.16 < z < 0.36$, while the $\text{H}\alpha$ line is redshifted outside the SDSS i -band filter above $z \sim 0.28$. The division into three subsamples of similar size is realized by applying cuts at $M_{5500-6800}^{\text{rest}} = -21.72$ mag and $M_{5500-6800}^{\text{rest}} = -22.33$ mag. We do not match the distribution of any other parameter for these subsamples. All samples used in this paper are presented in Table 1.

3.5. Defining the Optically Selected AGN Subsamples

The optically selected SDSS AGNs (called “quasars” in the SDSS literature) are drawn from the catalog provided by Schneider et al. (2010). Instead of using the classic selection in the B -band, Schneider et al. (2010) use the SDSS i -band, as it is less affected by Galactic absorption. However, this comes with the significant disadvantage that host-galaxy light might represent a significant fraction of the total flux in the i -filter. Schneider et al. (2010) apply an apparent magnitude cut of $M_i \leq -22$ and require that objects have at least one emission line exceeding an FWHM of 1000 km s^{-1} . Unlike our RASS/SDSS AGN sample, this sample of 3500 objects ($0.16 \leq z \leq 0.36$) has the footprint of SDSS Data Release 7. The DR4+ and DR7 areas are 5468 deg^2 and 7670 deg^2 , respectively, when we consider only the area that has a DR7 completeness ratio of $f_{\text{compl}} > 0.8$. Thus the area occupied by the optically selected AGN sample is 1.4 times larger than the area covered by the X-ray-selected AGN sample. Additionally, the number density (per square degree) of optically selected AGNs is 1.6 times higher than for the X-ray-selected AGNs.

We retrieve the individual SDSS spectra of the optically selected SDSS AGNs and derive the FWHM of the

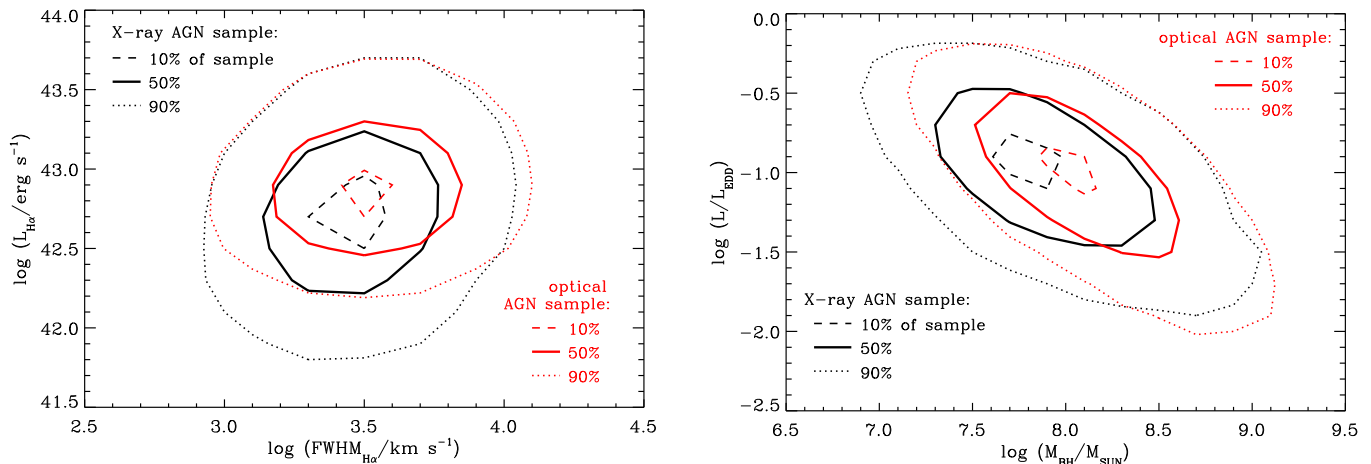


FIG. 6.— Comparison between the X-ray-selected RASS/SDSS AGNs (black lines) and the optically selected SDSS AGN samples (red lines). The contours show the location of 10% (dashed lines), 50% (solid lines), and 90% (dotted line) of the full sample, respectively. The left figure shows the observed parameters, luminosity and FWHM of the $H\alpha$ line, while the right figure shows the derived parameters L/L_{EDD} and M_{BH} . In both figures, a boxcar smoothing with a width of two has been applied.

broad $H\alpha$ line and the $L_{H\alpha}$ through spectral fits (see Sect. 3). This procedure is identical to the one used for the RASS/SDSS AGN sample (see Sect. 3.1). We select only objects with $S/N > 10$ in the flux of the broad $H\alpha$ line. We derive the individual black hole masses and L/L_{EDD} for the remaining 2831 AGNs. The X-ray and optically selected AGN samples have 807 objects in common, which is 29% of the total optically selected AGN sample. Thus, there is substantial difference between the X-ray and optically selected AGN samples.

Figure 6 compares how the X-ray-selected RASS/SDSS AGN sample and the optically selected SDSS AGN sample span the observed parameter space of $L_{H\alpha}$ and FWHM (left panel) and the derived parameter space of L/L_{EDD} and M_{BH} (right panel). In the observed parameter space, there are two obvious differences between these samples. First, the RASS/SDSS AGN sample extends to lower $L_{H\alpha}$. This is likely a consequence of rejecting AGNs with $M_i > -22$ in order to exclude objects with a strong starlight component from the host galaxy because an AGN has to have a certain luminosity to outshine its host galaxy. Clearly, X-ray selection of AGNs (RASS/SDSS) allows us to extend to fainter AGN luminosities, below the optical cut. Thus, at X-ray wavelengths we are able to detect AGNs that might not outshine their host galaxy in the optical (see, e.g., Hopkins et al. 2009). At $\log(L_{H\alpha}/[\text{erg s}^{-1}]) > 42.5$, both samples span a similar parameter space, and the dynamic range in FWHM is almost identical in both samples.

Differences in the observed parameter space naturally translate into differences in the derived $M_{\text{BH}}-L/L_{\text{EDD}}$ space (Fig. 6, right panel). Compared with the X-ray-selected AGN sample, the optical AGN sample has a deficiency of AGNs with low M_{BH} . The optically selected sample also extends marginally to higher M_{BH} and lower L/L_{EDD} .

We create optically selected AGN subsamples with respect to M_{BH} , L/L_{EDD} , FWHM, and $L_{H\alpha}$ (with matched distribution in the other parameter of interest; see Sect. 3.4). We have to use slightly different limits for some of the parameters because the X-ray

and optically selected AGN samples cover slightly different parameter spaces. Thus, when we create the low, medium, and high M_{BH} subsamples with matched L/L_{EDD} distributions, we use an L/L_{EDD} limit of $-2.3 < \log(L/L_{\text{EDD}}) < 0.1$. The optical M_{BH} subsamples have median $\langle \log(L/L_{\text{EDD}}) \rangle = -1.04$ to -1.00 , while the L/L_{EDD} subsamples have $\langle \log(M_{\text{BH}}/M_{\odot}) \rangle = 8.12 - 8.13$.

When we create three subsamples in FWHM, we limit $L_{H\alpha}$ to $42.1 < \log(L_{H\alpha}/[\text{erg s}^{-1}]) < 44.1$. The FWHM subsamples have $\langle \log(L_{H\alpha}/[\text{erg s}^{-1}]) \rangle = 42.88$. For the $L_{H\alpha}$ subsamples, we apply a limit of $2.8 < \log(\text{FWHM}/[\text{km s}^{-1}]) < 4.2$. We find $\langle \text{FWHM} \rangle = 3240 - 3280 \text{ km s}^{-1}$ for the low, medium, and high $L_{H\alpha}$ subsamples. All bin widths are identical to the ones used for defining the X-ray-selected AGN subsamples.

We produce optical AGN subsamples divided by M_i . We use simple M_i cuts of $M_i = -22.27$ and $M_i = -22.67$ to construct faint, medium, and luminous M_i subsamples with similar numbers of sources. Finally, we create $M_{5500-6800}^{\text{rest}}$ subsamples of the optically selected AGN. We use cuts at $M_{5500-6800}^{\text{rest}} = -22.13 \text{ mag}$ and $M_{5500-6800}^{\text{rest}} = -22.53 \text{ mag}$. As with the X-ray-selected AGNs, we do not match the distribution of any other parameter when creating the subsamples defined by M_i and $M_{5500-6800}^{\text{rest}}$. All samples are presented in Table 1.

4. METHODOLOGY

4.1. Clustering Measurements

We measure the two-point correlation function $\xi(r)$ (Peebles 1980), which measures the excess probability dP above a Poisson distribution of finding an object in a volume element dV at a distance r from another randomly chosen object. The ACF measures the spatial clustering of objects in the same sample, while the CCF measures the clustering of objects in two different samples. We use the same approach as described in detail in Section 3 of Paper I and Section 4 in Paper III. Here we explain the essential elements of our method.

We use the correlation estimator of Davis & Peebles

(1983) in the form

$$\xi(r) = \frac{DD(r)}{DR(r)} - 1, \quad (3)$$

where $DD(r)$ is the number of data–data pairs with a separation r , and $DR(r)$ is the number of data–random pairs. Both pair counts have been normalized by the number density of data and random points. To separate the effect of redshift distortions, the correlation function is measured as a function of two components of the separation vector between two objects, that is, one perpendicular to (r_p) and the other along (π) the line of sight. The parameter $\xi(r_p, \pi)$ is thus extracted by counting pairs on a two-dimensional grid of separations r_p and π . We obtain the projected correlation function $w_p(r_p)$ by integrating $\xi(r_p, \pi)$ along the π direction.

As in Paper I, we infer the AGN ACF from the CCF between AGN and the corresponding galaxy tracer set and the ACF of the tracer set following Coil et al. (2009):

$$w_p(\text{AGN}|\text{AGN}) = \frac{[w_p(\text{AGN}|\text{trace})]^2}{w_p(\text{trace}|\text{trace})}, \quad (4)$$

where $w_p(\text{AGN}|\text{AGN})$ and $w_p(\text{trace}|\text{trace})$ are the ACFs of the AGN and the corresponding tracer set, respectively, and $w_p(\text{AGN}|\text{trace})$ is the CCF between the AGN and the tracer set (i.e., a galaxy sample).

The CCF is computed using

$$\xi_{\text{AGN-trace}} = \frac{D_{\text{AGN}} D_{\text{trace}}}{D_{\text{AGN}} R_{\text{trace}}} - 1. \quad (5)$$

For our purposes, the use of this simple estimator has several major advantages and results in only a marginal loss in the S/N when compared to more advanced estimators (e.g., Landy & Szalay 1993). The estimator in Equation (5) requires the generation of a random catalog only for the tracer set. Since the random catalog should exactly match all observational biases to minimize the systematic uncertainties, well-understood selection effects are key to creating proper random samples. The tracer sets have well-defined selection functions, while the AGN samples suffer from selection functions that are very complex and difficult to model.

4.2. Error Analysis

The measurements in the adjacent bins of the correlation function are not independent. Poisson errors will significantly underestimate the uncertainties and should not be used for error calculations. Instead, we use the jackknife resampling technique to estimate the measurement errors based on the covariance matrix M_{ij} , which reflects the degree to which bin i is correlated with bin j .

In our jackknife resampling, we divide the survey area into $N_T = 100$ subsections for the DR4+ geometry (X-ray-selected AGN sample), each of which is $\sim 50\text{--}60 \text{ deg}^2$. Since the optically selected AGN sample uses the DR7 geometry, we divide this area into $N_T = 131$ subsections of roughly equal area. These N_T jackknife-resampled correlation functions define the covariance matrix:

$$M_{ij} = \frac{N_T - 1}{N_T} \left[\sum_{k=1}^{N_T} \left(w_k(r_{p,i}) - \langle w(r_{p,i}) \rangle \right) \right. \\ \left. \times \left(w_k(r_{p,j}) - \langle w(r_{p,j}) \rangle \right) \right] \quad (6)$$

We calculate $w_p(r_p)$ N_T times, where each jackknife sample excludes one section and $w_k(r_{p,i})$ and $w_k(r_{p,j})$ are from the k th jackknife samples of the AGN ACF and $\langle w(r_{p,i}) \rangle$, $\langle w(r_{p,j}) \rangle$ are the averages over all of the jackknife samples. The uncertainties represent 1σ (68.3%) confidence intervals.

The generation of the covariance matrix for the inferred AGN ACF considers the N_T jackknife-resampled correlation functions of the CCF (AGN and corresponding tracer set) and the tracer set ACF. For each jackknife sample, we calculate the inferred AGN ACF by using Equation 4. The resulting N_T $w_p(r_p)$ jackknife-resampled projected correlation functions of the inferred ACFs are then used to compute the covariance matrix of the inferred AGN ACF.

5. RESULTS

We measure high-accuracy CCFs of the different AGN samples with the LRG tracer set (see Fig. 7). In addition, we compute the high-precision ACF of the LRG sample. In both cases, we measure r_p in the range $0.05\text{--}40 \text{ h}^{-1}$ Mpc in 15 logarithmic bins, identical to those used in Paper III. We compute π in steps of 5 h^{-1} Mpc in the range $\pi = 0\text{--}200 \text{ h}^{-1}$ Mpc.

To derive π_{max} , we compute $w_p(r_p)$ for a set of π_{max} ranging from 10 to 160 h^{-1} Mpc in steps of 10 h^{-1} Mpc. We then fit $w_p(r_p)$ over an r_p range of $0.3\text{--}40 \text{ h}^{-1}$ Mpc with a fixed $\gamma = 1.9$ and determine the correlation length r_0 for the individual π_{max} measurements. As in Papers I–III, we find that the LRG ACF saturates at $\pi_{\text{max}} = 80 \text{ h}^{-1}$ Mpc. All CCFs saturate at $\pi_{\text{max}} = 40 \text{ h}^{-1}$ Mpc. Power-law fits for the ACFs and CCFs are based on

$$w_p(r_p) = r_p \left(\frac{r_0}{r_p} \right)^\gamma \frac{\Gamma(1/2)\Gamma((\gamma-1)/2)}{\Gamma(\gamma/2)}, \quad (7)$$

where $\Gamma(x)$ is the Gamma function.

To derive the clustering properties of the AGN samples, we follow two different approaches:

(1) Power-law fits to the inferred AGN ACF:

We use Eq. 4 to infer the ACF for the individual AGN sample from the CCF of this sample with the LRG tracer set and the ACF of the LRG sample. We fit the data points of the inferred AGN ACFs with the expression given in Eq. 7 and derive best-fit r_0 and γ values. The data are fitted over the range $r_p = 0.3\text{--}15 \text{ h}^{-1}$ Mpc to be consistent with Papers I–III. Since we measure the CCF to infer the ACF, the resulting effective redshift distribution for the clustering signal is determined by both the redshift distribution of the tracer set and the AGN sample: $N_{\text{CCF}}(z) = N_{\text{tracer}}(z) * N_{\text{AGN}}(z)$.

In Table 1 we list the redshift range, the median effective redshift of $N_{\text{CCF}}(z)$ for the corresponding AGN samples, the derived best r_0 and γ values based on power-law fits, and r_0 for a power-law fit with a fixed slope of $\gamma = 1.9$ (for ease of comparison).

(2) Bias from HOD modeling:

In Paper II we develop a novel method to infer the HOD of RASS/SDSS AGNs directly from the well-constrained CCF of RASS/SDSS AGNs with LRGs. In performing the HOD modeling,

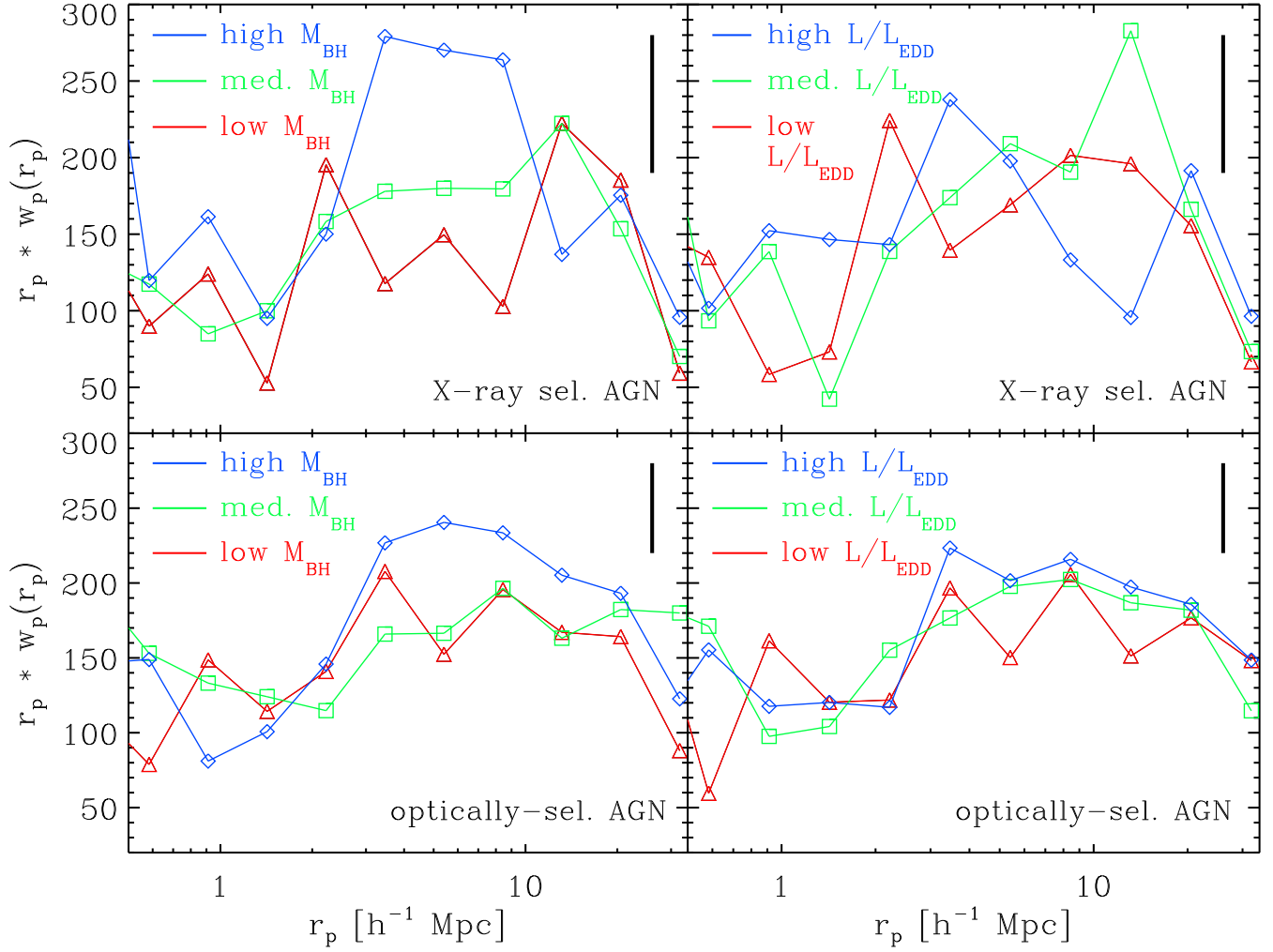


FIG. 7.— Directly measured cross-correlation functions between AGN subsamples for different parameters with matched distributions in the other parameter of interest. In the top row we show the results for the X-ray-selected AGNs, while the bottom row shows results for the optically selected AGNs. In each panel, the color encodes the low (red), medium (green), and high (blue) subsample in the corresponding parameter. For the sake of clarity, we show only a typical error bar in each panel (black solid vertical line in right upper corner of each panel). Note that we show on the y axis $r_p \times w_p(r_p)$ instead of $w_p(r_p)$ to allow for an easier comparison between the different subsamples and to make the values easier to read in the figure.

we consider that galaxies and AGNs are associated with DMHs. A DMH may contain one or more galaxies or AGNs that are included in our samples. Using the HOD of the LRGs as a template, we constrain the HOD of the AGN by fitting the CCF between AGNs and LRGs. A few of the CCFs do not have enough pairs on small scales for applying χ^2 statistics. Thus to derive consistent constraints for all CCF, we consider only bins with $r_p > 0.7 h^{-1} \text{ Mpc}$ for all CCF fits (as in Paper III).

Using the best-fit model of the AGN HODs, we derive the bias parameter of the AGN sample by applying

$$b_{\text{AGN}} = \frac{\int b_h(M_h) \langle N_{\text{AGN}} \rangle (M_h) \phi(M_h) dM_h}{\int \langle N_{\text{AGN}} \rangle (M_h) \phi(M_h) dM_h}, \quad (8)$$

where $b_h(M_h)$ is the bias of DMHs with a mass M_h , and $\phi(M_h)$ is the DMH mass function. In Paper II, we discuss different realizations of the HOD modeling depending on how central and satellite AGNs in DMHs are included or excluded. Here, we apply only “Model A,” assuming that, at low redshifts, black hole accretion occurs more frequently in galaxies with lower stellar mass than in typ-

ical LRGs. Thus, we assume that (1) the LRG (highest stellar mass) occupies the center of the DMH and (2) all AGNs are satellites within the same DMH. This is motivated by observations of AGN “downsizing” (Ueda et al. 2003; Hasinger 2008; Miyaji et al. 2015).

As we are interested here (and in Paper III) only in the large-scale bias values and the estimate of the typical halo mass, our results do not depend significantly on the choice of the one-halo term model (model A, B, or C). For example, in the case of the total RASS AGN sample, the best-fit HOD-derived bias values change by less than 0.02 among models A, B, and C. This is a minor fraction of the statistical uncertainty in the bias measurement (± 0.09).

The bias parameters derived by power-law fits and HOD modeling can deviate significantly. As discussed in Paper III (see Section 5.4. of Paper III for more details), HOD-derived bias parameters are strongly preferred over those from power-law fits for various reasons.

Inconsistencies between the HOD-derived $b(z)$ and the results from power-law fits are caused by (1) obtaining power-law fits to the inferred AGN ACFs, which have

TABLE 1
PROPERTIES OF INFERRED AGN ACFs AND DERIVED QUANTITIES

AGN Sample Name	Number of Objects	Median z_{eff}	10th,50th,90th Percentile	r_0 (h^{-1} Mpc)	γ	$r_{0,\gamma=1.9}$ (h^{-1} Mpc)	$b(z)$ HOD	$\log M_{\text{DMH}}^{\text{typ}}$ ($h^{-1} M_{\odot}$)
X-ray Selected AGN — RASS/SDSS AGN — SDSS Data Release 4+								
total RASS AGN	1349	0.27	43.70,44.17,44.68	$4.02^{+0.45}_{-0.57}$	$1.62^{+0.15}_{-0.14}$	$4.09^{+0.35}_{-0.39}$	$1.32^{+0.11}_{-0.09}$	$13.20^{+0.13}_{-0.13}$
low L_X RASS	858	0.25	43.63,43.99,44.23	$3.12^{+0.57}_{-0.89}$	$1.55^{+0.25}_{-0.21}$	$3.28^{+0.41}_{-0.46}$	$1.22^{+0.14}_{-0.12}$	$13.08^{+0.19}_{-0.20}$
high L_X RASS	491	0.29	44.34,44.53,44.87	$5.38^{+0.68}_{-0.87}$	$1.88^{+0.18}_{-0.18}$	$5.41^{+0.65}_{-0.73}$	$1.53^{+0.15}_{-0.17}$	$13.41^{+0.13}_{-0.18}$
<i>low M_{BM} RASS</i>	410	0.22	7.07,7.54,8.01	$2.71^{+0.53}_{-1.11}$	$2.07^{+1.46}_{-0.64}$	$2.65^{+0.56}_{-0.71}$	$0.96^{+0.24}_{-0.12}$	$12.60^{+0.48}_{-0.39}$
<i>medium M_{BM} RASS</i>	525	0.27	7.55,7.92,8.36	$4.34^{+0.64}_{-0.90}$	$1.61^{+0.19}_{-0.18}$	$4.32^{+0.52}_{-0.58}$	$1.38^{+0.15}_{-0.17}$	$13.27^{+0.16}_{-0.23}$
<i>high M_{BM} RASS</i>	400	0.29	7.92,8.38,8.91	$4.60^{+0.82}_{-1.11}$	$1.85^{+0.21}_{-0.22}$	$4.67^{+0.78}_{-0.92}$	$1.62^{+0.20}_{-0.16}$	$13.49^{+0.16}_{-0.15}$
<i>low L/L_{EDD} RASS</i>	418	0.23	-1.79,-1.36,-0.98	$3.00^{+0.78}_{-1.20}$	$1.45^{+0.26}_{-0.21}$	$3.17^{+0.54}_{-0.64}$	$1.30^{+0.18}_{-0.18}$	$13.21^{+0.21}_{-0.27}$
<i>medium L/L_{EDD} RASS</i>	522	0.27	-1.36,-1.00,-0.71	$2.87^{+1.97}_{-1.50}$	$1.59^{+0.40}_{-0.33}$	$2.89^{+0.46}_{-0.54}$	$1.29^{+0.13}_{-0.15}$	$13.16^{+0.16}_{-0.23}$
<i>high L/L_{EDD} RASS</i>	404	0.29	-1.01,-0.68,-0.35	$4.36^{+0.67}_{-0.79}$	$2.14^{+0.22}_{-0.19}$	$3.92^{+0.74}_{-0.89}$	$1.18^{+0.15}_{-0.14}$	$12.97^{+0.22}_{-0.26}$
<i>low FWHM RASS</i>	415	0.27	1280,1910,2470	$2.69^{+0.61}_{-0.80}$	$2.30^{+0.72}_{-0.40}$	$2.32^{+0.71}_{-1.01}$	$1.09^{+0.12}_{-0.17}$	$12.84^{+0.20}_{-0.27}$
<i>medium FWHM RASS</i>	525	0.26	2340,2890,3690	$2.90^{+1.25}_{-0.32}$	$1.35^{+0.24}_{-0.25}$	$3.70^{+0.64}_{-0.76}$	$1.47^{+0.17}_{-0.17}$	$13.38^{+0.16}_{-0.21}$
<i>high FWHM RASS</i>	404	0.27	3650,4840,7920	$3.52^{+0.32}_{-1.57}$	$1.53^{+0.25}_{-0.26}$	$3.82^{+0.65}_{-0.77}$	$1.53^{+0.17}_{-0.18}$	$13.43^{+0.15}_{-0.20}$
<i>low $L_{\text{H}\alpha}$ RASS</i>	414	0.22	41.99,42.29,42.53	$2.14^{+0.96}_{-1.72}$	$1.39^{+0.56}_{-0.32}$	$2.69^{+0.54}_{-0.68}$	$1.21^{+0.18}_{-0.19}$	$13.10^{+0.23}_{-0.35}$
<i>medium $L_{\text{H}\alpha}$ RASS</i>	526	0.27	42.52,42.74,42.96	$1.96^{+1.00}_{-1.97}$	$1.83^{+1.32}_{-0.36}$	$2.13^{+0.64}_{-0.71}$	$1.31^{+0.16}_{-0.16}$	$13.18^{+0.19}_{-0.24}$
<i>high $L_{\text{H}\alpha}$ RASS</i>	403	0.29	42.93,43.22,43.63	$3.52^{+0.92}_{-1.57}$	$1.53^{+0.25}_{-0.26}$	$3.82^{+0.65}_{-0.78}$	$1.36^{+0.18}_{-0.16}$	$13.23^{+0.19}_{-0.23}$
faint M_i RASS	444	0.23	-21.26,-21.80,-22.04	$3.21^{+0.69}_{-1.58}$	$1.69^{+0.69}_{-0.42}$	$3.32^{+0.58}_{-0.70}$	$1.10^{+0.26}_{-0.14}$	$12.90^{+0.39}_{-0.31}$
medium M_i RASS	460	0.27	-22.15,-22.39,-22.63	$3.51^{+0.71}_{-1.16}$	$1.71^{+0.36}_{-0.29}$	$3.65^{+0.61}_{-0.72}$	$1.21^{+0.19}_{-0.16}$	$13.04^{+0.25}_{-0.29}$
luminous M_i RASS	445	0.29	-22.76,-23.13,-23.96	$3.04^{+0.76}_{-1.12}$	$1.47^{+0.17}_{-0.18}$	$2.94^{+0.54}_{-0.65}$	$1.48^{+0.17}_{-0.16}$	$13.36^{+0.16}_{-0.19}$
faint $M_{5500-6800}^{\text{rest}}$ RASS	444	0.22	-20.84,-21.39,-21.66	$3.18^{+0.63}_{-1.12}$	$1.79^{+0.56}_{-0.41}$	$3.19^{+0.59}_{-0.71}$	$1.13^{+0.25}_{-0.19}$	$12.97^{+0.35}_{-0.42}$
med. $M_{5500-6800}^{\text{rest}}$ RASS	460	0.27	-21.79,-22.02,-22.27	$2.44^{+1.15}_{-1.94}$	$1.36^{+0.29}_{-0.28}$	$3.39^{+0.57}_{-0.67}$	$1.25^{+0.16}_{-0.17}$	$13.10^{+0.20}_{-0.28}$
lum. $M_{5500-6800}^{\text{rest}}$ RASS	445	0.30	-22.42,-22.81,-23.67	$4.23^{+0.76}_{-1.00}$	$1.70^{+0.15}_{-0.16}$	$4.20^{+0.67}_{-0.79}$	$1.44^{+0.16}_{-0.17}$	$13.31^{+0.15}_{-0.21}$
Optically Selected AGN — SDSS AGN — SDSS Data Release 7								
total SDSS AGN	2831	0.29	-22.08,-22.45,-23.34	$5.07^{+0.26}_{-0.28}$	$1.80^{+0.09}_{-0.09}$	$5.06^{+0.25}_{-0.26}$	$1.32^{+0.07}_{-0.06}$	$13.18^{+0.08}_{-0.09}$
faint M_i SDSS	932	0.28	-22.03,-22.13,-22.24	$5.34^{+0.42}_{-0.51}$	$1.80^{+0.20}_{-0.18}$	$5.34^{+0.40}_{-0.33}$	$1.47^{+0.09}_{-0.09}$	$13.36^{+0.09}_{-0.14}$
medium M_i SDSS	966	0.29	-22.30,-22.45,-22.63	$3.79^{+0.41}_{-0.59}$	$1.73^{+0.18}_{-0.16}$	$3.97^{+0.38}_{-0.39}$	$1.20^{+0.08}_{-0.10}$	$13.00^{+0.19}_{-0.17}$
luminous M_i SDSS	933	0.30	-22.73,-23.06,-23.86	$4.48^{+0.51}_{-0.64}$	$1.63^{+0.12}_{-0.12}$	$4.52^{+0.41}_{-0.45}$	$1.40^{+0.12}_{-0.12}$	$13.26^{+0.13}_{-0.15}$
<i>low M_{BM} SDSS</i>	857	0.27	7.37,7.82,8.35	$4.24^{+0.46}_{-0.56}$	$1.74^{+0.15}_{-0.15}$	$4.26^{+0.41}_{-0.45}$	$1.28^{+0.12}_{-0.13}$	$13.14^{+0.15}_{-0.20}$
<i>medium M_{BM} SDSS</i>	1114	0.30	7.70,8.08,8.59	$4.97^{+0.40}_{-0.48}$	$1.98^{+0.17}_{-0.18}$	$4.88^{+0.41}_{-0.44}$	$1.18^{+0.13}_{-0.09}$	$12.96^{+0.19}_{-0.16}$
<i>high M_{BM} SDSS</i>	845	0.31	8.04,8.45,8.97	$4.72^{+0.63}_{-0.82}$	$1.50^{+0.12}_{-0.12}$	$4.76^{+0.43}_{-0.47}$	$1.60^{+0.10}_{-0.08}$	$13.45^{+0.09}_{-0.07}$
<i>low L/L_{EDD} SDSS</i>	859	0.28	-1.84,-1.31,-0.88	$3.40^{+0.55}_{-0.77}$	$1.58^{+0.14}_{-0.15}$	$3.62^{+0.39}_{-0.44}$	$1.21^{+0.11}_{-0.10}$	$13.03^{+0.16}_{-0.17}$
<i>medium L/L_{EDD} SDSS</i>	1113	0.30	-1.53,-1.04,-0.67	$4.68^{+0.58}_{-0.73}$	$1.62^{+0.13}_{-0.13}$	$4.89^{+0.43}_{-0.46}$	$1.40^{+0.11}_{-0.11}$	$13.26^{+0.12}_{-0.14}$
<i>high L/L_{EDD} SDSS</i>	845	0.31	-1.17,-0.74,-0.40	$4.75^{+0.60}_{-0.78}$	$1.64^{+0.14}_{-0.15}$	$4.73^{+0.50}_{-0.55}$	$1.49^{+0.15}_{-0.12}$	$13.35^{+0.14}_{-0.13}$
<i>low FWHM SDSS</i>	857	0.30	1490,2110,2560	$4.18^{+0.49}_{-0.56}$	$1.92^{+0.19}_{-0.19}$	$4.17^{+0.49}_{-0.55}$	$1.11^{+0.13}_{-0.08}$	$12.84^{+0.21}_{-0.17}$
<i>medium FWHM SDSS</i>	1120	0.29	2680,3260,4040	$5.03^{+0.43}_{-0.53}$	$1.75^{+0.13}_{-0.13}$	$5.12^{+0.38}_{-0.40}$	$1.41^{+0.10}_{-0.09}$	$13.28^{+0.11}_{-0.11}$
<i>high FWHM SDSS</i>	847	0.29	4300,5500,8460	$4.62^{+0.50}_{-0.63}$	$1.68^{+0.14}_{-0.14}$	$4.71^{+0.42}_{-0.46}$	$1.44^{+0.10}_{-0.12}$	$13.32^{+0.10}_{-0.15}$
<i>low $L_{\text{H}\alpha}$ SDSS</i>	859	0.27	42.40,42.61,42.71	$3.72^{+0.51}_{-0.73}$	$1.63^{+0.16}_{-0.17}$	$3.79^{+0.41}_{-0.45}$	$1.25^{+0.13}_{-0.08}$	$13.10^{+0.17}_{-0.12}$
<i>medium $L_{\text{H}\alpha}$ SDSS</i>	1119	0.30	42.76,42.89,43.04	$4.25^{+0.49}_{-0.68}$	$1.69^{+0.15}_{-0.16}$	$4.47^{+0.39}_{-0.42}$	$1.32^{+0.13}_{-0.10}$	$13.16^{+0.15}_{-0.14}$
<i>high $L_{\text{H}\alpha}$ SDSS</i>	846	0.31	43.07,43.26,43.63	$4.52^{+0.61}_{-0.80}$	$1.56^{+0.14}_{-0.14}$	$4.50^{+0.46}_{-0.51}$	$1.52^{+0.13}_{-0.13}$	$13.38^{+0.12}_{-0.14}$
faint $M_{5500-6800}^{\text{rest}}$ SDSS	933	0.27	-21.70,-21.97,-22.10	$5.96^{+0.41}_{-0.44}$	$1.88^{+0.13}_{-0.14}$	$5.95^{+0.40}_{-0.43}$	$1.50^{+0.09}_{-0.11}$	$13.40^{+0.09}_{-0.15}$
med. $M_{5500-6800}^{\text{rest}}$ SDSS	964	0.30	-22.17,-22.31,-22.49	$3.36^{+0.71}_{-1.18}$	$1.55^{+0.20}_{-0.22}$	$3.96^{+0.40}_{-0.45}$	$1.14^{+0.10}_{-0.11}$	$12.89^{+0.16}_{-0.22}$
lum. $M_{5500-6800}^{\text{rest}}$ SDSS	934	0.31	-22.59,-22.89,-23.66	$4.57^{+0.55}_{-0.66}$	$1.69^{+0.13}_{-0.13}$	$4.56^{+0.48}_{-0.53}$	$1.46^{+0.12}_{-0.13}$	$13.32^{+0.12}_{-0.12}$

NOTE. — Samples displayed in italics are those that are created to match distributions in the other parameter of interest (e.g, samples split in M_{BM} have matched distributions in L/L_{EDD} and vice versa; samples split in FWHM have matched distributions in $L_{\text{H}\alpha}$). The fourth column lists either the log ($L_X/[\text{erg s}^{-1}]$), log (M_{BM}/M_{\odot}), log (L/L_{EDD}), FWHM (km s^{-1}), log ($L_{\text{H}\alpha}/[\text{erg s}^{-1}]$), absolute magnitude in the i -band (M_i in mag), or absolute rest-frame magnitude in the 5500–6800 Å band ($M_{5500-6800}^{\text{rest}}$ in mag) of the studied sample. In this column, the 50th percentile corresponds to the median value. For the total sample, we state in this column the L_X or the M_i value. All samples cover a redshift range of $0.16 < z < 0.36$ and contain only objects with S/N > 10 in H α flux. Values of r_0 , γ , and $r_{0,\gamma=1.9}$ are obtained from a power-law fit to $w_p(r_p)$ over the range $r_p = 0.3\text{--}15 h^{-1}$ Mpc, using the full error covariance matrix and minimizing the correlated χ^2 values.

much larger uncertainties than the directly measured CCFs between AGNs and LRGs (the HOD uses CCFs instead of the AGN ACFs), and (2) fitting the inferred AGN ACF in a range $r_p = 0.3\text{--}15 h^{-1}$ Mpc. The latter is also applied by other studies because the clustering signal is not well constrained above $r_p \sim 15 h^{-1}$ Mpc. However, such a fit includes scales in the nonlinear region in which the bias-DMH mass relation, based on linear theory, should not be applied. We decide to do so nevertheless to be consistent with Papers I and III, as well to allow the reader to perform a direct comparison to other studies.

Based on the HOD-derived bias parameter ($b(z)$ HOD), we derive the typical DMH mass occupied by the AGN sample. Using Equation (8) of Sheth et al. (2001) and the improved fit for this equation given by Tinker et al. (2005), we compute the expected large-scale Eulerian bias factor for different DMH masses at different redshifts. Comparing the observed b value from HOD modeling with the DMH bias factor from Λ CDM cosmological simulations provides an estimate of the typical DMH mass ($b_{\text{DMH}}(M_{\text{DMH}}^{\text{typ}}) = b_{\text{OBS,HOD}}$) in which the different AGN samples reside, as listed in the last column of Table 1. Small differences in the median effective redshift between different subsamples do not significantly change the derived typical DMH mass. The low and high M_{BH} samples of the X-ray-selected AGN sample have the largest difference in median effective redshift when we consider only samples that have matched distributions in the other parameter of interest. Computing the typical DMH mass at these different redshifts leads to a difference of only $\Delta \log(M_{\text{DMH}}^{\text{typ}}) = 0.08$ (e.g., for a bias value of 1.20, $\log(M_{\text{DMH},z=0.22}^{\text{typ}}/[h^{-1} M_{\odot}]) = 12.83$ and $\log(M_{\text{DMH},z=0.30}^{\text{typ}}/[h^{-1} M_{\odot}]) = 12.75$).

We emphasize that $M_{\text{DMH}}^{\text{typ}}$ should *not* be compared between different studies. Various conversions are used in the literature to derive $M_{\text{DMH}}^{\text{typ}}$ from b_{DMH} . In particular, *for the same bias parameter*, studies based on optically selected AGN samples derive $M_{\text{DMH}}^{\text{typ}}$ values up to ~ 0.6 dex lower than studies using X-ray-selected AGN samples (depending on the actual bias factor and redshift of the sample). The use of the improved fit from Tinker et al. (2005) compared to Equation (8) of Sheth et al. (2001) alone can account for an $M_{\text{DMH}}^{\text{typ}}$ difference of ~ 0.3 dex. Thus, instead of blindly using the derived $M_{\text{DMH}}^{\text{typ}}$ values from different studies, one should recompute these values from the bias parameters in the same manner.

For the X-ray and optically selected AGN samples, we find a clustering dependence on M_{BH} , in that subsamples with high M_{BH} cluster more strongly than their low M_{BH} counterparts. No significant clustering dependence on L/L_{EDD} is observed. We also detect a weak $\text{FWHM}_{\text{H}\alpha}$ clustering dependence, in that AGN with low $\text{FWHM}_{\text{H}\alpha}$ are less clustered than their high $\text{FWHM}_{\text{H}\alpha}$ counterparts. For the X-ray AGN sample, which has a larger dynamical range in $L_{\text{H}\alpha}$ than the optical sample, we do not find a significant dependence on $L_{\text{H}\alpha}$.

5.1. Robustness of the Clustering Measurements

In this section we verify the reliability of our clustering results by altering the selection of the different AGN subsamples with respect to different parameters. Mod-

erate changes should not influence the clustering results significantly. Therefore this should serve as a test of the robustness of our results.

In Section 3.2, we clarify why we do not use black hole mass estimates from objects with $\text{H}\alpha$ luminosity $S/N < 10$. For the first check, we lower this threshold to $S/N=5$, generate the various AGN subsamples, and compute their clustering. Comparing the subsamples with respect to the same parameter (e.g., X-ray luminosity, M_{BH} , L/L_{EDD}), the newly derived constraints agree well within their 1σ uncertainties with the findings of the $S/N=10$ samples. The same applies when we apply a very conservative threshold of $S/N=20$.

The intrinsic scatter of approximately 0.3 dex in the SMBH mass estimate could have a substantial effect on the observed correlations between M_{DMH} and M_{BH} as well as L/L_{EDD} . In Section 6.4, we use simulations to explore the impact of SMBH mass errors on the clustering correlations and show that the expected modification of the correlations is very mild.

In this section, we investigate possible effects of the scatter in the SMBH mass estimates from the observational point of view. Two different approaches for estimating M_{BH} based on the optical spectra were discussed in Section 3.2. Throughout the paper, we use the relation given in Bentz et al. (2009) (see Eq. 2). Here we recompute M_{BH} based on McLure & Dunlop (2004) (see Eq. 1). For the X-ray and optically selected AGN samples, the M_{BH} values estimated from McLure & Dunlop (2004) are on average 0.2 dex smaller than the ones from Bentz et al. (2009). We repeat the clustering measurement of low and high M_{BH} and L/L_{EDD} AGN subsamples, respectively. We find trends identical to those reported in Table 1. The results for all subsamples based on McLure & Dunlop (2004) agree well with their corresponding subsamples based on Bentz et al. (2009), within the 1σ uncertainties. Thus, different estimators for the SMBH mass, which are subject to different systematic errors, give extremely similar results. We conclude that, in our study, uncertainties related to the clustering measurement itself (i.e., the moderate number of AGNs) dominate over systematic SMBH mass errors.

A key ingredient of our paper is that we split the AGN sample in such a way that we match the distribution of another parameter of interest (see Sect. 3.4). To test this, we alter the procedure of creating the different subsamples. First, we fit a regression line to the data and split the sample into objects above and below the regression line. The resulting subsamples have moderately deviating distributions in the other parameter of interest. This approach yields consistent clustering results with respect to our final results presented in Table 1.

Second, we repeat the generation of low, medium, and high M_{BH} and L/L_{EDD} samples with matched distributions in the other parameter of interest. This time, we split the sample into 40% (low), 20% (medium), and 40% (high). All corresponding samples agree with the original samples, within the combined 1σ uncertainties. Except for the optical L/L_{EDD} subsamples, we also find identical trends for all other parameters in the X-ray and optically selected AGN samples. For the optical L/L_{EDD} subsamples, the split into 30% (low), 40% (medium), and 30% (high) suggests a weak and tentative positive L/L_{EDD} clustering dependence ($\sim 1.7\sigma$ between the low and high

L/L_{EDD} subsamples; see Table 1). When we split the same sample into 40% (low), 20% (medium), and 40% (high), we find $b_{\text{low}} = 1.35^{+0.11}_{-0.10}$, $b_{\text{medium}} = 1.33^{+0.17}_{-0.16}$, and $b_{\text{high}} = 1.35^{+0.14}_{-0.11}$. Thus, we find no evidence for an L/L_{EDD} clustering dependence.

Third, we generate subsamples that have perfectly identical distributions in the other parameter of interest (instead of very similar distributions). To do so, we compute in each bin which of the subsamples (low, medium, or high) contains the most objects. We then randomly select and add again objects from the subsamples with the lower number of objects until all three subsamples contain an equal number of objects in this bin. In other words, we scale up the number of objects in a subsample to that of the subsample with the highest number of objects. This method allows multiple entries of single objects in a given subsample. Ultimately, in each bin only one or two objects are added to subsamples. Thus, these subsamples are extremely similar to the matched samples that we use throughout the paper. Consequently, it is not surprising that both methods result in virtually identical clustering signals.

In Fig. 5 (right panel histogram) the low, medium, and high M_{BH} subsamples overlap considerably. As a fourth test, we now create low and high M_{BH} and L/L_{EDD} subsamples that have completely separated distributions, but still match in the L/L_{EDD} and M_{BH} distribution, respectively. We divide the X-ray and optical AGN samples at $M_{\text{BH}} = 10^8 M_{\odot}$ and $\log(L/L_{\text{EDD}}) = -1$. We weight the samples by adding sources in a subsample multiple times until a matched distribution is created. One major disadvantage of this approach is that we have to limit substantially the parameter space of the other parameter to match its distribution in both subsamples (see Figs. 4, 5). For the X-ray-selected RASS/SDSS AGN samples, we find $b_{\text{low}M_{\text{BH}}} = 1.05^{+0.18}_{-0.16}$, $b_{\text{high}M_{\text{BH}}} = 1.26^{+0.21}_{-0.20}$, $b_{\text{low}L/L_{\text{EDD}}} = 1.13^{+0.18}_{-0.18}$, and $b_{\text{high}L/L_{\text{EDD}}} = 1.17^{+0.16}_{-0.14}$. The bias values for the optically selected SDSS AGN samples are $b_{\text{low}M_{\text{BH}}} = 1.26^{+0.14}_{-0.16}$, $b_{\text{high}M_{\text{BH}}} = 1.38^{+0.16}_{-0.15}$, $b_{\text{low}L/L_{\text{EDD}}} = 1.32^{+0.10}_{-0.13}$, and $b_{\text{high}L/L_{\text{EDD}}} = 1.28^{+0.21}_{-0.21}$. Due to significant restriction of the parameter space and thus a substantial decrease in the number of AGN, this approach leads to less significant results.

Fifth, we combine the X-ray and optically selected AGN samples. We divide the combined sample into the highest 30%, middle 40%, and lowest 30% with respect to the corresponding parameter. We also combine the middle and lowest samples (70%). Again, the different subsamples have matched distributions in the other parameter of interest. We find a 2.6σ difference when comparing the AGNs with the 30% highest to the 70% lowest SMBH masses ($b_{70\%\text{low}M_{\text{BH}}} = 1.19^{+0.07}_{-0.08}$, $b_{\text{high}M_{\text{BH}}} = 1.50^{+0.14}_{-0.10}$).

Last, we drop the requirement of having subsamples with matched distributions in the other parameter of interest. We naively create samples of low, medium, and high M_{BH} , L/L_{EDD} , FWHM, and $L_{\text{H}\alpha}$ simply by dividing the samples into the highest 30%, medium 40%, and lowest 30% with respect to the corresponding parameter. Dividing the sample according to M_{BH} , for example, in this manner leads to subsamples with very different median L/L_{EDD} values. We present the results for subsam-

TABLE 2
CLUSTERING PROPERTIES WITH RESPECT TO M_{BH} AND L/L_{EDD}
WHEN USING UNMATCHED DISTRIBUTIONS IN THE OTHER
PARAMETER OF INTEREST

AGN Sample Name	Median log (M_{BH}/M_{\odot})	Median log (L/L_{EDD})	$b(z)$ HOD
X-ray-selected RASS/SDSS AGN – Data Release 4+			
low M_{BH} RASS	7.49	-0.76	$1.00^{+0.18}_{-0.15}$
medium M_{BH} RASS	7.92	-1.01	$1.36^{+0.20}_{-0.18}$
high M_{BH} RASS	8.46	-1.33	$1.49^{+0.15}_{-0.16}$
low L/L_{EDD} RASS	8.29	-1.42	$1.41^{+0.17}_{-0.16}$
medium L/L_{EDD} RASS	7.92	-1.00	$1.49^{+0.20}_{-0.15}$
high L/L_{EDD} RASS	7.62	-0.64	$1.09^{+0.10}_{-0.12}$
Optically Selected AGN – SDSS AGN – SDSS Data Release 7			
low M_{BH} SDSS	7.72	-0.72	$1.28^{+0.11}_{-0.16}$
medium M_{BH} SDSS	8.12	-1.04	$1.15^{+0.08}_{-0.07}$
high M_{BH} SDSS	8.58	-1.42	$1.58^{+0.07}_{-0.06}$
low L/L_{EDD} SDSS	8.51	-1.46	$1.43^{+0.11}_{-0.10}$
medium L/L_{EDD} SDSS	8.08	-1.03	$1.42^{+0.11}_{-0.12}$
high L/L_{EDD} SDSS	7.76	-0.65	$1.12^{+0.15}_{-0.06}$

NOTE. — An explanation of the columns is given in Table 1.

ples in M_{BH} and L/L_{EDD} with unmatched distributions in the other parameter (for X-ray and optical AGN) in Table 2. Despite the “mixing” of the two parameters, M_{BH} and L/L_{EDD} , the trends seen in the HOD-based bias parameters are similar, though not identical, to the subsamples with matched distributions. We will discuss these results below in Sect. 6.1 in more detail.

As described above, we consider only data bins for all CCFs with $r_p > 0.7 h^{-1}$ Mpc for the computation of the HOD-based bias parameter. As a last test, we recompute the HOD bias parameter using bins with $r_p > 0.5 h^{-1}$ Mpc. Again, the results agree well within the 1σ uncertainties. The few exceptions are caused by a very low data point at $r_p \sim 0.6 h^{-1}$ Mpc. In all of these cases, there are at most 10 pairs that contribute to this data point. Thus, χ^2 statistics, as mentioned before, should not be applied. The combination of the various tests listed here provides convincing evidence that our results are not significantly influenced by systematic effects and demonstrates their robustness with respect to moderate changes in our methodology and sample selection.

5.2. Exploring the One-halo Term Dependence of Different AGN Parameters

The HOD modeling introduced in Paper II of this series allows us to explore properties of the one-halo term, that is, at small separations where two objects occupy the same DMH. More importantly, we are able to provide the full distribution of the number of AGNs as a function of M_{DMH} , instead of quoting only a typical value. As a parameterization of the AGN HOD, we use a simple truncated power law, assuming that all AGNs are in satellites (‘Model A’ in Paper II, for more details see Paper II):

$$\langle N_{\text{AGN},s} \rangle \propto M_{\text{DMH}}^{\alpha} \Theta(M_{\text{DMH}} - M_{\text{cr}}) \quad (9)$$

where $\Theta(x)$ is the step function ($=1$ at $x \geq 0$; $=0$ at $x < 0$), M_{cr} is a critical (minimum) DMH mass below

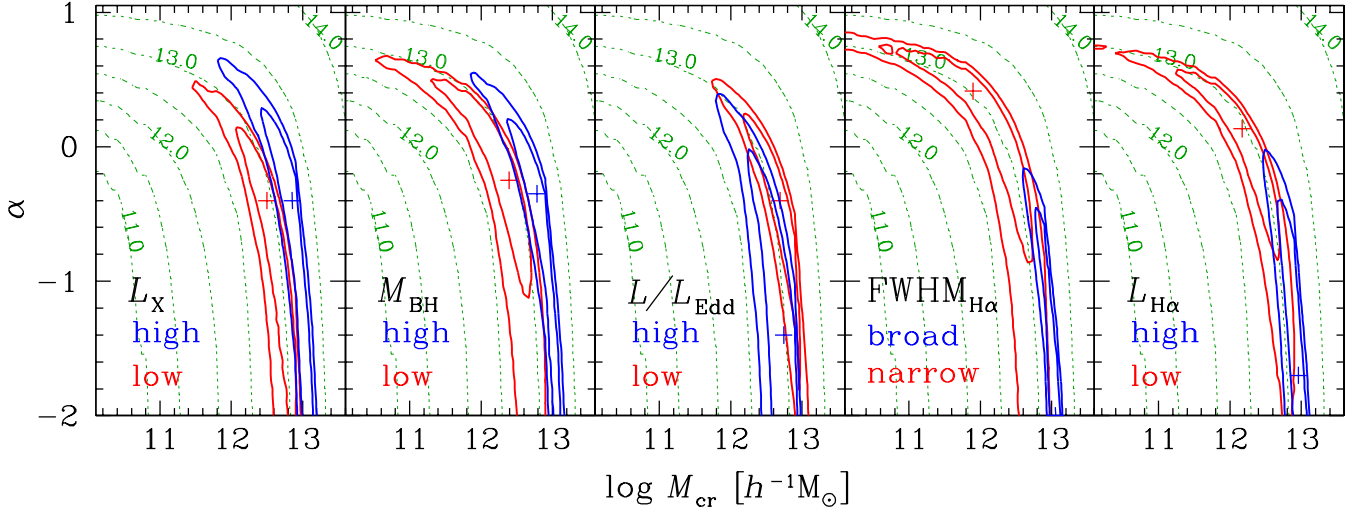


FIG. 8.— Confidence contours of the HOD-derived parameters α and $\log M_{\text{cr}}$ for the low and high L_X , M_{BH} , L/L_{Edd} , FWHM, and $L_{\text{H}\alpha}$ RASS/SDSS (X-ray-selected) luminous, broad-line AGN subsamples (from left to right). The blue contours show the high AGN subsamples in one parameter, and the red contours show the low subsamples. The confidence intervals correspond to the $\Delta\chi^2 = 1.0$ and 2.3 levels. The green dashed lines show the mean DMH mass in $\log(M_{\text{DMH}}/h^{-1}M_{\odot})$ derived from the model parameters. Every other contour level is labeled.

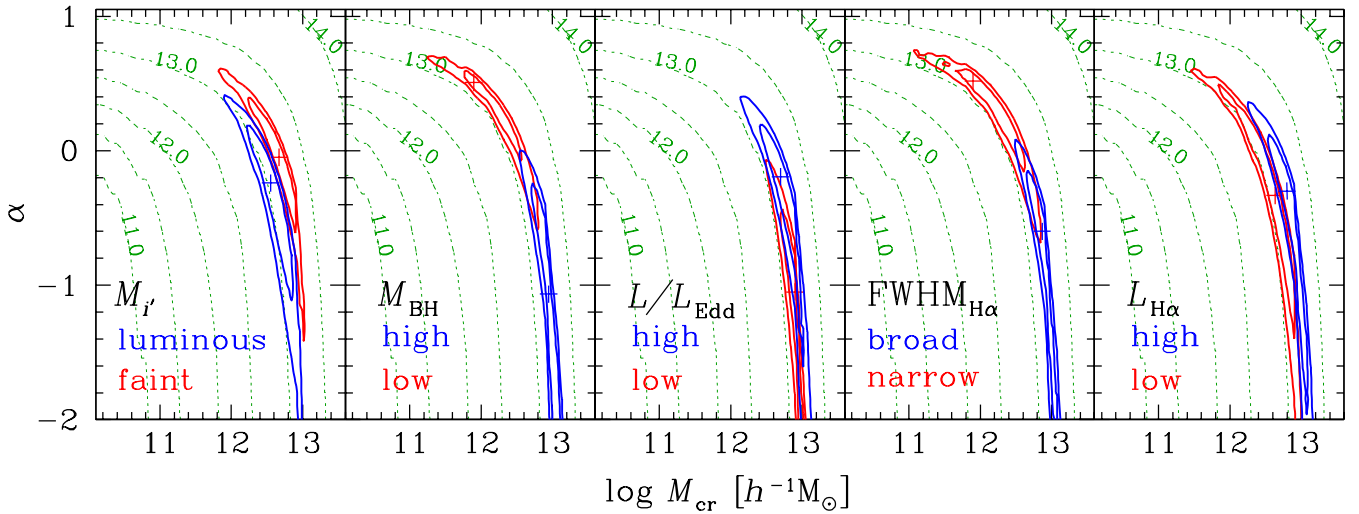


FIG. 9.— Similar to Fig. 8, here showing the confidence contours of the HOD parameters α and $\log M_{\text{cr}}$ for the low and high M_i , M_{BH} , L/L_{Edd} , FWHM, and $L_{\text{H}\alpha}$ optically selected SDSS AGN samples (from left to right).

which the HOD is zero (where the DMH does not contain an AGN), α is the power-law slope of the HOD above M_{cr} , and $N_{\text{AGN},s}$ the number of (satellite) AGNs in the same DMH.

While a model with an adequate mix of central and satellite AGNs is more realistic (models B and C in Paper II), we here show the results of our simplest model because the purpose of this section is to highlight the differences between samples, including the constraints from both the one- and two-halo terms, while the constraints on bias values come only from the two-halo term.

To achieve adequate constraints, we divide the full AGN sample into only two subsamples (instead of three, as above) for each parameter of interest. We follow the description of Sect. 3.4 and create low and high samples for M_{BH} , L/L_{Edd} , FWHM, and $L_{\text{H}\alpha}$ with matched

distributions in L/L_{Edd} , M_{BH} , $L_{\text{H}\alpha}$, and FWHM, respectively. We list their clustering properties in Table 3. The low and high L_X and M_i samples use a simple cut ($\log(L_{0.1-2.4\text{keV}}/[\text{ergs}^{-1}]) = 44.29$, $M_i = -22.4$). For the faint M_i sample ($\langle M_i \rangle = -22.18$), we find $b_{\text{faint}} = 1.45^{+0.10}_{-0.12}$, while the luminous M_i sample ($\langle M_i \rangle = -22.79$) yields $b_{\text{lum.}} = 1.29^{+0.07}_{-0.10}$ (1.2σ difference). The M_i clustering dependence will be discussed in detail in Sect. 6.3.

We run the HOD modeling for all low and high AGN subsamples using bins with $r_p > 0.5 h^{-1}$ Mpc. To do so, we assume that χ^2 statistics can be applied if a data point contains at least 15 pairs. Lowering the r_p limit allows us to explore the one-halo term via HOD modeling in more detail. We derive the best fit for all of the low and high parameters individually and show their results

TABLE 3
CLUSTERING PROPERTIES WITH RESPECT TO M_{BH} AND L/L_{EDD} FOR
DIVISIONS INTO TWO SUBSAMPLES WITH MATCHED DISTRIBUTIONS

AGN Sample Name	Median z_{eff}	Median log (M_{BH}/M_{\odot})	Median log (L/L_{EDD})	$b(z)$ HOD
X-ray selected AGN – RASS/SDSS AGN – SDSS Data Release 4+				
low M_{BH}	0.24	7.66	-1.00	$1.14^{+0.13}_{-0.14}$
high M_{BH}	0.29	8.23	-1.00	$1.42^{+0.15}_{-0.15}$
low L/L_{EDD}	0.25	7.93	-1.24	$1.30^{+0.15}_{-0.13}$
high L/L_{EDD}	0.28	7.92	-0.77	$1.28^{+0.13}_{-0.14}$
		Median FWHM	Median log $L_{\text{H}\alpha}$	
low FWHM	0.26	2170	42.72	$1.15^{+0.19}_{-0.12}$
high FWHM	0.27	4050	42.72	$1.47^{+0.13}_{-0.13}$
low $L_{\text{H}\alpha}$	0.24	2890	42.45	$1.15^{+0.16}_{-0.14}$
high $L_{\text{H}\alpha}$	0.29	2890	43.04	$1.44^{+0.13}_{-0.14}$
Optically Selected AGN – SDSS AGN – SDSS Data Release 7				
low M_{BH}	0.28	7.89	-1.02	$1.29^{+0.09}_{-0.10}$
high M_{BH}	0.30	8.32	-1.04	$1.43^{+0.10}_{-0.09}$
low L/L_{EDD}	0.28	8.12	-1.22	$1.38^{+0.08}_{-0.09}$
high L/L_{EDD}	0.30	8.12	-0.83	$1.38^{+0.09}_{-0.11}$
		Median FWHM	Median log $L_{\text{H}\alpha}$	
low FWHM	0.26	2440	42.88	$1.27^{+0.10}_{-0.08}$
high FWHM	0.27	4550	42.88	$1.45^{+0.08}_{-0.11}$
low $L_{\text{H}\alpha}$	0.24	3250	42.69	$1.30^{+0.09}_{-0.10}$
high $L_{\text{H}\alpha}$	0.29	3280	43.10	$1.42^{+0.09}_{-0.09}$

NOTE. — An explanation of the columns is given in Table 1. The units of FWHM are kms^{-1} and $\log L_{\text{H}\alpha}$ are $\log(L_{\text{H}\alpha}/[\text{ergs}^{-1}])$. Note that the units and column descriptions of the optically selected SDSS AGNs are identical to the ones used for the X-ray-selected RASS/SDSS AGNs.

in Figs. 8 and 9. These two-dimensional plots show a clearer difference between the subsamples than collapsing the information into one dimension such as the bias parameter.

All low and high subsamples (independent of the studied parameter) are consistent with $\alpha < 1$. As pointed out in Paper II, HOD analyses of galaxies over a wide range of absolute magnitudes and redshifts find $\alpha \sim 1.0$ – 1.2 . Comparing the AGN and galaxy results implies that models are preferred in which the fraction of satellite AGNs to satellite galaxies decreases with increasing DMH mass. Fig. 8 shows evidence that high FWHM and broad-line $L_{\text{H}\alpha}$ AGNs show an even steeper decrease with DMH mass (i.e., lower α).

The confidence contours of the optically selected AGN subsamples (Fig. 9) are narrower than for the X-ray-selected sample. This is due to the larger number of optical AGNs than X-ray-selected AGNs. However, the general two-dimensional appearance of the confidence contours are very similar between the X-ray and optically selected AGN samples. We note that, for the M_{BH} subsamples, the low and high optically selected AGNs have different α and M_{cr} values, while the low and high M_{BH} X-ray-selected AGN subsamples have consistent α and different M_{cr} values.

6. DISCUSSION

In this section, we use our results to discuss the physical origin of the observed L_X clustering dependence. We also compare our results to other studies and discuss why we do not detect an M_i clustering dependence when the clustering results between the X-ray and optical AGN samples are so similar. Finally, we compare our results to predictions from state-of-the-art semianalytic cosmological simulations.

6.1. M_{BH} as the Origin of the L_X Clustering Dependence

We first verify that the weak X-ray luminosity dependence of the clustering strength found in Paper I is still present in the reduced AGN sample when we exclude $\sim 13\%$ of all objects to reliably estimate M_{BH} . The dependence is detected at the 1.4σ level when considering “ $b(z)$ HOD” in Table 1 (and is 2.5σ comparing the r_0 values at fixed γ). Using the full X-ray sample, we reported a 1.8σ detection in Paper II using HOD-derived bias values.

We split the X-ray-selected AGN sample into three subsamples with respect to M_{BH} (with matched L/L_{EDD} distributions) and show the results in Fig. 10 (left) as a blue line. The X-ray sample shows a steady increase of the bias parameter with M_{BH} . The difference between the lowest and highest M_{BH} subsamples in the X-ray-selected AGN sample is 2.3σ .

For the X-ray and optically selected AGN sample (red line), we detect the highest clustering in the subsample that contains the 30% most massive black holes. For both AGN populations, we combine the low and the medium subsamples and compute their combined clustering strength. As a result of the increased sample size, the uncertainties decrease. The bias difference compared to the high M_{BH} subsample is 2.0σ and 2.7σ for the X-ray and optical AGN samples, respectively. We show these data points at the median M_{BH} values of each subsample in Fig. 10.

The X-ray AGN sample shows no hints of a correlation between clustering strength and L/L_{EDD} (Fig. 10, right panel). The optical AGN sample has a slight positive correlation in that AGNs with higher L/L_{EDD} cluster are slightly more clustered than their lower L/L_{EDD} counterparts. However, this $\sim 1.7\sigma$ difference disappears when we split the sample into 40% (low), 20% (medium), and 40% (high) bins in L/L_{EDD} (see Fig. 10, right panel). In Sect. 6.3 below we discuss the nonnegligible selection biases of the optical SDSS AGN sample; as a result, we regard the X-ray-selected AGN sample as less contaminated by observational selection effects. Thus, we do not find convincing statistical evidence for a clustering dependence with L/L_{EDD} .

For the X-ray-selected AGNs, we still detect a 2.0σ difference between the low and high M_{BH} samples when we do not require that the subsamples have matched distributions in L/L_{EDD} . Using simple cuts in L/L_{EDD} without required matched distributions in M_{BH} yields a 2.2σ difference in that low and medium L/L_{EDD} AGNs cluster more strongly than high L/L_{EDD} AGNs. If we assume that this L/L_{EDD} AGN clustering dependence is real and that there is no clustering dependence on M_{BH} , this finding would contradict the observed X-ray lumi-

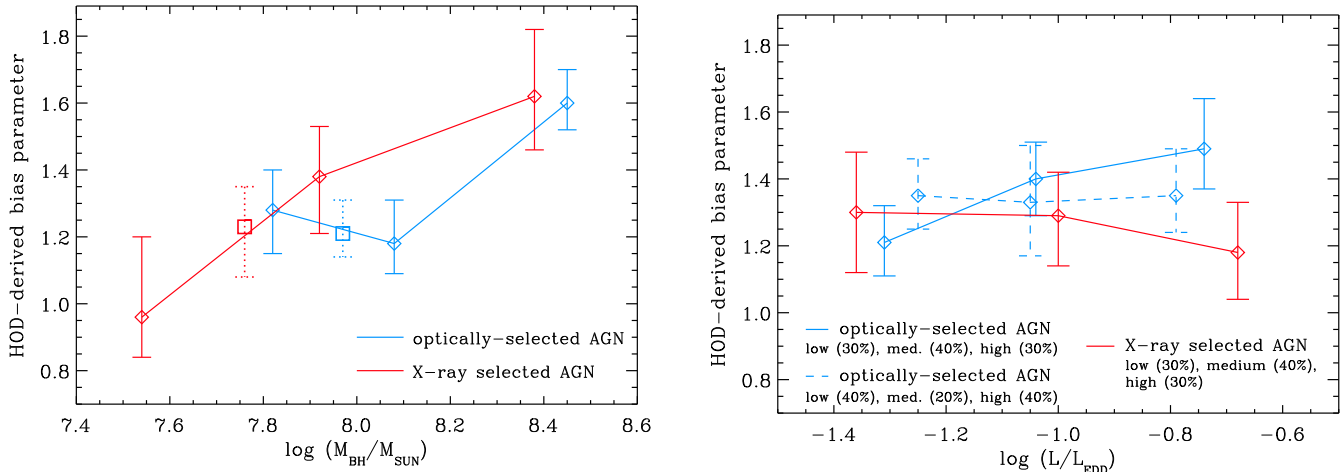


FIG. 10.— *Left*: HOD-derived bias parameter as a function of SMBH mass for the optically selected SDSS (blue) and the X-ray-selected RASS/SDSS AGN sample (red). The diamond points show a division of the full sample in M_{BH} into 30% high, 40% medium, and 30% low M_{BH} subsamples. The boxes (with dotted error bars) indicate the combined medium and low M_{BH} of the corresponding subsample.

Right: similar to the left panel, showing the HOD-derived bias parameter as a function of Eddington ratio. For the optically selected AGN sample, we display the division of the full sample into 30% high, 40% medium, and 30% low (solid blue line) and the division into 40% high, 20% medium, and 40% low (dashed blue line). For the sake of clarity, for the X-ray-selected AGN sample we show only the division into 30% high, 40% medium, and 30% low, which is extremely similar to the other divisions for this sample.

nosity clustering dependence that high L_X AGNs (and thus high L/L_{EDD}) are more strongly clustered than low L_X AGNs. Figures 4 and 5 show that the AGNs with the lowest L/L_{EDD} AGN also have high M_{BH} . Thus, we conclude that differences in M_{BH} (in these naively defined subsamples) are responsible for the observed differences in the clustering of the low and high L/L_{EDD} AGN subsamples. Similar results are found for the optically selected AGN sample when we do simple divisions of the full sample without matching the distributions in the other parameter of interest.

Since M_{BH} is estimated from the observed parameters FWHM and $L_{\text{H}\alpha}$, we also investigate the dependence of the clustering strength when we divide the full samples according to these parameters (see Table 1). As before, we divide the sample in one parameter in such a way that we conserve the distribution in the other parameter in all subsamples. In our sample of luminous broad-line (X-ray-selected) RASS/SDSS AGNs, we find a 2.0σ clustering difference between the lowest and highest FWHM samples and only a 0.6σ difference between the lowest and highest $\text{H}\alpha$ luminosity samples. For the optical AGN sample, we find a 1.9σ difference for the low and high FWHM samples and a 1.5σ difference for the low and high $\text{H}\alpha$ luminosity samples. Both parameters are used to estimate M_{BH} , though the scaling is much stronger with FWHM than with $L_{\text{H}\alpha}$ (converted to L_{5100} , see Equations 1 and 2). The similar FWHM clustering dependence in the X-ray and optical AGN samples provides further evidence that M_{BH} is the key parameter driving the observed L_X dependence of the clustering strength.

Analysis of the two-dimensional parameter space in Fig. 8 further supports our claim that the L_X dependence of the clustering strength originates from an M_{BH} dependence. For the X-ray-selected sample (Fig. 8), the contours of the low and high M_{BH} samples are extremely similar to the L_X contours, while the L/L_{EDD} contours differ significantly from the L_X contours. We therefore

conclude that only the black hole mass, and not a combination of M_{BH} and L/L_{EDD} , is responsible for the observed weak X-ray luminosity dependence of the clustering. Within the explored M_{BH} range, we estimate an average increase of the bias parameter of $\Delta b \sim 0.7$ per dex M_{BH} . This corresponds to approximately one dex increase in M_{DMH} per dex M_{BH} .

If our studies had shown that the clustering strength correlates directly with L/L_{EDD} but not with M_{BH} , then more strongly clustered AGNs would accrete more material. In this scenario, because highly accreting AGNs would lie in environments with a high density of galaxies, galaxy mergers and galaxy-galaxy interactions would likely be the main triggers of AGN activity. However, we find that the clustering strength depends mainly on M_{BH} and not on L/L_{EDD} . Thus, high X-ray luminosity AGNs do not necessarily require dense environments to accrete more matter. We find that, on average, AGNs in dense environments have higher M_{BH} than their counterparts in lower density environments. The higher L_X that are observed are then a direct consequence of having higher M_{BH} .

Our findings are also consistent with a scenario in which the AGN luminosity can vary on short timescales (e.g., Hickox et al. 2014), due to a variability in the black hole accretion rate (L/L_{EDD}). In this view, the instantaneous luminosity of an AGN is only a weak indicator of the time-averaged black hole accretion rate. Since L/L_{EDD} (which reflects the amount of accreted gas) can rapidly fluctuate, it will not necessarily show a correlation with the properties of the host galaxy or DMH mass. On the other hand, M_{BH} cannot fluctuate on short timescales as it stays nearly constant or grows slowly. Therefore, the black hole mass is not subject to stochastic variability and correlates more tightly with host galaxy properties and the host DMH mass.

In the hierarchical model of structure formation, more massive galaxies reside in more massive DMHs (e.g.,

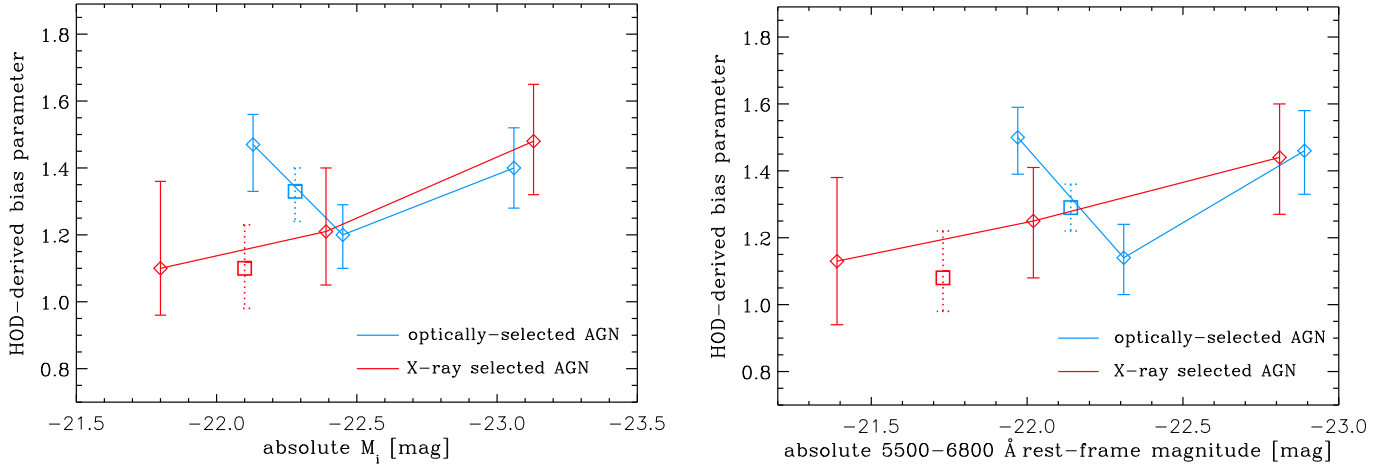


FIG. 11.— Similar to Fig. 10. *Left*: HOD-derived bias parameter as a function of absolute SDSS M_i magnitude for low (33%), medium (34%), and high (33%) subsamples. *Right*: HOD-derived bias parameter as a function of absolute rest-frame magnitude in the 5500–6800 Å band. The data points shown with a box (with uncertainties shown as dotted lines) correspond to the samples created by combining the low and medium absolute 5500–6800 Å rest-frame magnitude subsamples.

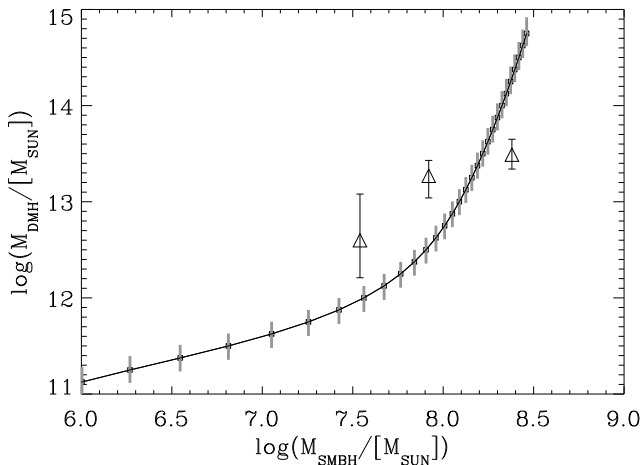


FIG. 12.— Simple model prediction of the relation between the dark matter halo mass and SMBH mass, using Behroozi et al. (2013) and Conroy & White (2013). This simple model does not include any potential effects that an AGN can have on the host galaxy or host halo. The gray error bars of the correlation reflect the observational errors in the data used to derive the Behroozi et al. (2013) relationship between stellar mass and M_{DMH} . The triangles show our clustering results for the X-ray-selected AGN sample when we divide the full sample into low, medium, and high M_{BH} samples.

Mostek et al. 2013; Skibba et al. 2015). More massive galaxies are also more luminous (e.g., Tully & Fisher 1977; McGaugh et al. 2000). This leads to the well-observed luminosity dependence of the clustering signal for galaxies (e.g., Zehavi et al. 2011; Skibba et al. 2014). If more massive galaxies also had more massive bulges, the relationship between the M_{BH} and stellar velocity dispersion of the surrounding galactic bulge (e.g., Ferrarese & Merritt 2000; Gebhardt et al. 2000; Kormendy & Ho 2013) should then also lead to a correlation of M_{BH} and M_{DMH} .

We first compare our results with a simple empirically motivated model, rather than a full semianalytic model. We take the relations between galaxy stellar mass and DMH mass at $z \sim 0.3$ from Behroozi et al. (2013). Next, we assign each galaxy a black hole with a mass that is determined by the stellar mass of the host galaxy, follow-

ing Conroy & White (2013) (their Eq. 1). No scatter in the stellar mass to M_{BH} relationship is included in our treatment.

The result of this simple model is shown in Fig. 12, along with our measurements. There are discrepancies between the model prediction and measurements: at $M_{\text{BH}} < 10^8 M_{\odot}$ the model predicts a lower M_{DMH} than we find, though the difference is within 3σ . At higher M_{BH} , the model predicts a stronger relationship between M_{BH} and M_{DMH} than we find. While it is understandable how our measurements could lie about the predicted line, in that we measure the mass of the parent halo from the large-scale bias while the model predicts the mass of the subhalo hosting the AGN, our measurement at $M_{\text{BH}} \sim 10^{8.4} M_{\odot}$ falls below the prediction (a 3.7σ difference).

The shallower slope seen in the data compared to the model here could be caused by the cumulative scatter in each of the correlations in the logical chain ($M_{\text{DMH}} \rightarrow M_{\text{stellar}} \rightarrow M_{\text{bulge}} \rightarrow M_{\text{BH}}$). We will evaluate the predictions of semianalytic models in Sect. 6.4 and will show that they describe our findings better than the simple model does.

6.2. Comparing Our Results to Other Studies

Zhang et al. (2013) and Komiya et al. (2013) study the projected quasar number density around galaxies. Both find evidence that the clustering scale length r_0 depends on M_{BH} . Zhang et al. (2013) detects this trend, however, at a significance level of only $\sim 1\sigma$. They also note that there is no clustering dependence on optical quasar luminosity. Based on SDSS AGN data, Komiya et al. (2013) find a trend that r_0 increases with $M_{\text{BH}} > 10^8 M_{\odot}$. Our r_0 measurements for the M_{BH} subsamples (although at moderately different redshift ranges) agree with their results when we consider the 1σ uncertainties. At lower black hole masses, Komiya et al. (2013) do not find an r_0 dependence. This might be due to selection biases of the AGN population, as we will show below in Sect. 6.4. Additionally, Komiya et al. (2013) do not find significant r_0 dependences on AGN luminosity (L_{5100}). However, the dynamic range in their study is less than a magnitude.

Shen et al. (2009) compute the ACF of optically selected broad-line SDSS AGNs (DR5) at $0.4 \leq z \leq 2.5$. They detect a $\sim 2\sigma$ difference in the clustering strength when they split the AGN sample into the 10% most massive M_{BH} and the remaining 90%, in that AGNs with the highest M_{BH} are more strongly clustered. Their results are consistent with our findings, although their sample extends up to $z = 2.5$ and contains more massive black holes at higher redshifts. When Shen et al. (2009) split their sample into luminous and faint quasars, they found that both correlation functions agree with each other. Only the 10% most luminous quasars show a larger clustering strength (at the $\sim 2\sigma$ level) than the remaining 90% of the sample. This result is also consistent with our findings, which we will discuss in the next subsection (see also Fig. 11, left).

6.3. Why Do We Not Detect an M_i Clustering Dependence in the Optically Selected AGN Sample?

Interestingly, we find very similar clustering dependences for the X-ray and the optically selected AGN samples. However, an important question remains: if there are such similar dependences in the clustering strength with M_{BH} , L/L_{EDD} , FWHM, and $L_{\text{H}\alpha}$, why do we not see a clustering dependence with M_i when we see a dependence with L_{X} ? Within the X-ray-selected sample, we detect a very weak M_i clustering dependence, in that the faint and luminous M_i RASS AGN samples (see Table 1) differ by 1.2σ . The direct comparison between the M_i clustering dependence of the X-ray and optically selected sample in Fig. 11 (left) shows that only the faint optical M_i subsamples deviate from the trend detected in the X-ray-selected sample. However, the difference is not significant considering the uncertainties of the measurements.

Above $z \sim 0.28$ the $\text{H}\alpha$ line is shifted outside the SDSS i -band filter. The redshift range studied here includes sources above and below this redshift. Thus, below $z \sim 0.28$ the broad-line $\text{H}\alpha$ line contributes flux to the M_i band, while above $z \sim 0.28$ this direct AGN luminosity indicator is not contributing to the M_i band flux. To explore if this difference in M_i contribution is responsible for the observed clustering difference in X-ray and optically selected AGN samples, we derive the absolute 5500–6800 Å rest-frame magnitude for all X-ray and optically selected AGN. The band pass of this rest-frame magnitude is chosen in such a way that it includes the $\text{H}\alpha$ line for all objects in our samples. We compute the clustering dependence as a function of this rest-frame absolute magnitude (Fig. 11, right) and find trends very similar to those as a function of M_i (Fig. 11, left). Thus, shifting the $\text{H}\alpha$ line outside the M_i band does not explain the difference in the clustering signals.

Figure 13 shows that the luminous absolute magnitude subsamples for the X-ray and optically selected AGN cover a similar parameter space in the M_{BH} versus absolute 5500–6800 Å rest-frame magnitude plane. The median values of the samples are almost identical. Thus, it is not very surprising that these samples have similar clustering strengths given their similar values of M_i , $\text{H}\alpha$, and absolute 5500–6800 Å rest-frame magnitude. On the other hand, Fig. 13 demonstrates that the faint ab-

solute magnitude subsamples for the X-ray and optically selected AGN samples are substantially different. The X-ray sample extends (as in all other parameters) to much lower magnitudes. Thus, the dynamic range of the X-ray-selected RASS/SDSS sample is wider than that of the optical AGN sample. As a consequence, the medium absolute magnitude subsample of the X-ray-selected AGN sample includes the vast majority of the optical AGN in the faint absolute magnitude subsample. If one combines the faint and medium absolute magnitude subsamples in the optical to roughly match the medium X-ray subsample, the clustering strength between both AGN populations agrees very well ($b_{\text{opt,faint+med.}} = 1.29_{-0.07}^{+0.07}$; see Fig. 11).

Finally, we explore the selection of the X-ray and optical AGNs in more detail. The RASS/SDSS sample is an X-ray flux-limited sample. *ROSAT*'s soft energy range significantly biases the sample toward broad-line AGNs as these sources are unabsorbed (or only mildly absorbed) in the X-rays. In addition to the X-ray flux limit, the sample is also subject to an optical flux limit because an SDSS spectrum is required for the characterization of a source. However, the X-ray and optical luminosities of broad-line AGNs correlate well (e.g., Tananbaum et al. 1979; Grupe et al. 2010; Lusso et al. 2010). Since *ROSAT* has limited sensitivity, it is able to detect only the X-ray-brightest AGNs. These objects are typically also bright in the optical. Thus, the impact of the optical flux limit on the sample selection is moderate.

The optical SDSS AGN selection, on the other hand, is much more complex. The target selection relies on several different selection techniques. The main criterion is a color cut and an optical flux limit. Broad-line AGNs with a certain amount of extinction will not meet the color-cut criterion. Additional objects are included in the sample due to their radio emission. Most importantly, an absolute magnitude cut is applied.

Figure 14 (left) shows that the optically selected AGN sample is not a flux-limited sample, although the sample selection considers only objects with $15.0 < i < 19.1$. The absolute M_i cut (applied to prevent substantial contamination by host galaxy light) causes a serious deficiency of objects above the lower i -band limit of $i < 19.1$. The X-ray-selected AGN sample (Fig. 14, right) includes objects down to almost the same apparent i -band magnitude, independent of redshift. Various SDSS papers discuss how the optical SDSS AGN sample is not a uniformly selected sample (e.g., Richards et al. 2006b). We conclude that the complex optical AGN selection might be the origin of the clustering differences between the X-ray and optically selected AGN samples. The strongest differences are detected between the samples of the lowest median redshift; this is also the range in which the optical AGN sample deviates most from a clean, flux-limited sample. We therefore consider the X-ray-selected RASS/SDSS AGN sample as the more complete sample and use only their clustering properties in the next section.

6.4. Comparison to cosmological simulations

Hydrodynamical (e.g., Bryan et al. 2014; Hirschmann et al. 2014; Steinborn et al. 2015) and semianalytical (e.g., Malbon et al. 2007; Marulli et al.

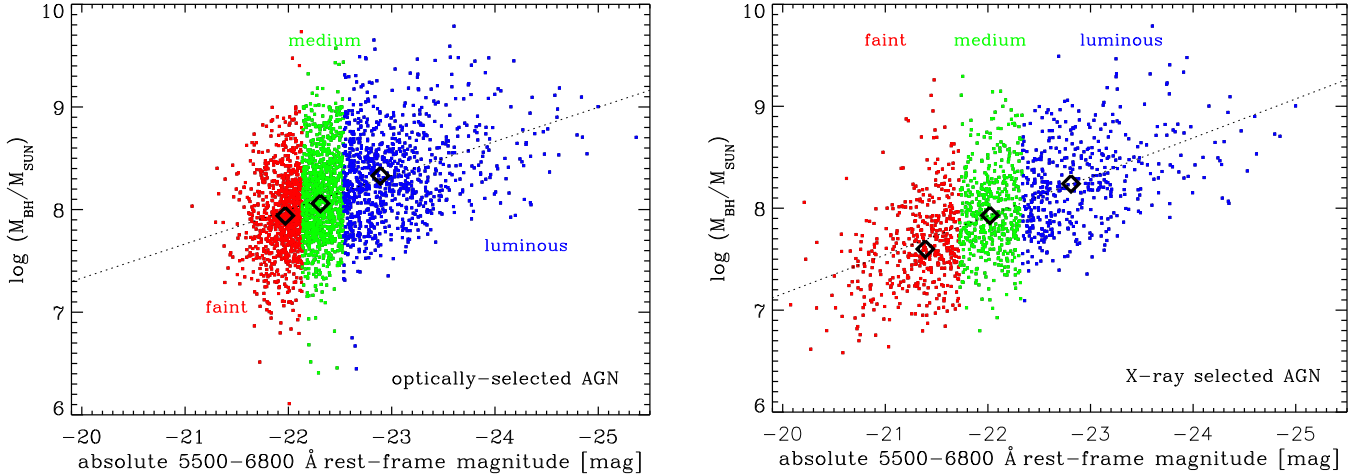


FIG. 13.— Black hole mass for optically selected SDSS (left) and X-ray-selected RASS/SDSS (right) AGNs vs. absolute 5500–6800 Å rest-frame magnitude. Different colors denote the division of the full samples into faint (33%), medium (34%), and luminous (33%) objects with respect to the rest-frame absolute magnitude. The black diamonds show the median absolute magnitude and median M_{BH} of the subsamples. We also show linear regression line fits to the full samples as dotted lines.

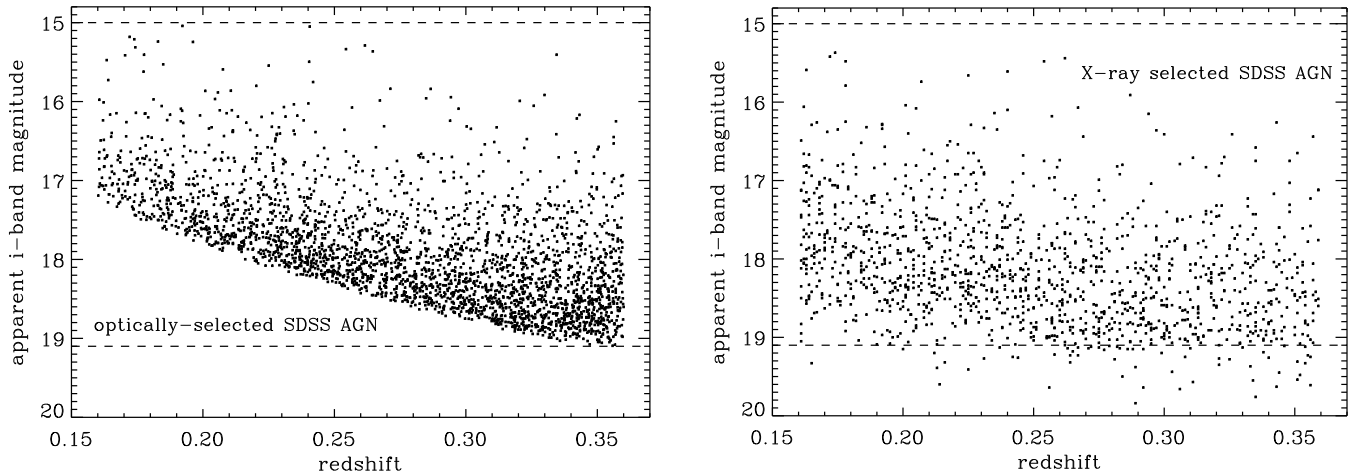


FIG. 14.— Apparent SDSS i -band magnitude vs. redshift for optically selected AGNs (left panel) and X-ray-selected AGNs (right panel). The horizontal dashed lines represent the lower and upper i -band limits for the selection of optical SDSS AGNs.

2008; Fanidakis et al. 2011; Benson 2012) state-of-the-art simulations have reached a level of complexity such that they can well predict observed quantities such as luminosity and stellar mass functions (e.g., Hopkins et al. 2006; Degraf et al. 2010; Fanidakis et al. 2012). The observed clustering properties of galaxies and AGNs provide additional important constraints for such models (e.g., Bonoli et al. 2009).

Theoretical models of galaxy formation that include prescriptions for modeling BH growth can provide important constraints on the fueling modes of AGN. For example, models in which AGN activity is triggered by major mergers between galaxies or secular processes within the host galaxy (e.g., disk instabilities) predict a well-defined correlation function for luminous quasars, with an average DMH mass of $M_{\text{DMH}} \sim 10^{12} h^{-1} M_{\odot}$ (Bonoli et al. 2009, 2010; Fanidakis et al. 2013). However, the inclu-

sion of an additional mode of growth that is linked to diffuse gas accretion in massive halos (Fanidakis et al. 2012) predicts a much higher average halo mass for moderate-luminosity AGNs, in contrast to their luminous counterparts (Fanidakis et al. 2013). Comparing this specific picture of AGN clustering with the available observations could potentially provide important insights into the correct modeling of the growth of black holes in galaxy-formation models.

Cosmological simulations and their predicted clustering properties can be also be used to test the impact of sample selection biases for observed samples. As an example, let us assume that in an unbiased sample there is no clustering dependence as a function of a certain AGN parameter. A particular observational selection bias might cause a clustering dependence to be measured. As selection biases can be included in the cosmological

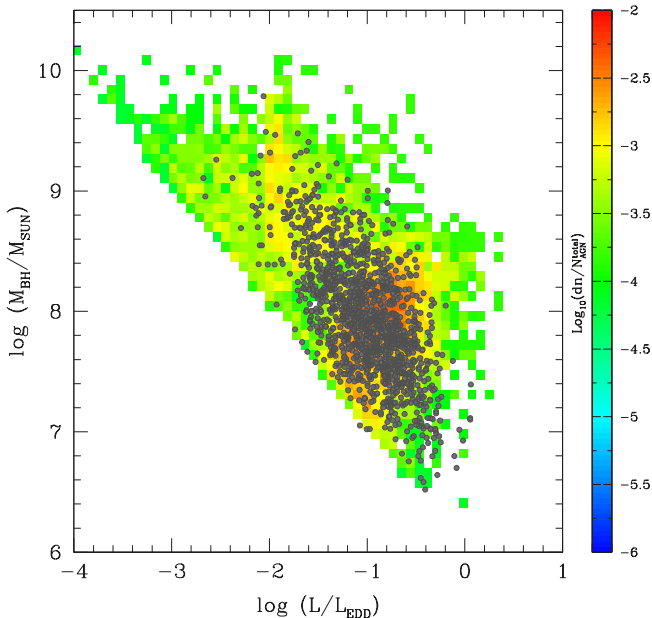


FIG. 15.— Eddington ratio vs. mass of the SMBH of simulated (color) and observed (gray) X-ray-selected AGNs. The color denotes the number of AGNs above the RASS flux limit divided by the total number of AGNs in the simulation, after applying the RASS flux limit. The gray data points indicate the location of the observed X-ray-selected RASS/SDSS AGN sample (see Fig. 5).

simulation, one can therefore compare the predictions for the unbiased and observed (including selection biases) AGN samples. Such knowledge is crucial to avoid wrong interpretations about the underlying physics when using clustering studies. Thus cosmological simulations are not only important to test our theoretical understanding of the observed universe but also to explore the impact of observational sample biases.

Here we use the semianalytical galaxy formation model GALFORM (Cole et al. 2000) to compare with our observed AGN clustering signals. Fanidakis et al. (2011, 2012, 2013) modeled SMBH in these simulations, using an identical model in all three papers. Only the cosmology has changed from WMAP1 (in the first two papers) to WMAP7 (Fanidakis et al. 2013). In Fanidakis et al. (2013), the authors incorporate two modes of AGN accretion in the GALFORM model. The first is the starburst mode (cold accretion), in which accretion onto the BH is tightly coupled to the mass of the cold gas available in the galaxy, which also contributes to star formation. This mode occurs when the host galaxy encounters a major galaxy merger, a minor merger, or a disk instability. These phenomena can take place in a wide range of halo masses. However, observable AGN luminosities within the range defined in this study are typically produced in DMHs with $M_{\text{DMH}} < 10^{12.5} h^{-1} M_{\odot}$ (Fanidakis et al. 2013).

The second is the hot-halo mode (hot accretion), which occurs in DMHs with higher masses. A fraction of the AGN energy output is used to heat the gas in the DMH and suppress cooling of the gas. The SMBH accretes directly from the diffuse gas in the DMH. This mode regulates the black hole accretion in very massive halos with $M_{\text{DMH}} \gtrsim 10^{13} h^{-1} M_{\odot}$. For more details on both modes and their modeling, we refer the reader to Fanidakis et al. (2013) and the references within.

The model of Fanidakis et al. (2013) is successful in reproducing several observational constraints, including the observed luminosity functions of galaxies and AGNs over a wide range of redshifts (Fanidakis et al. 2011, 2012). In addition, they can reproduce reasonably well the observed $M_{\text{BH}}-M_{\text{Gal,bulge}}$ relationship and the global and active black hole mass functions.

The primary motivation for running the simulation is to explore how AGN clustering depends on the mode of AGN accretion, as described in the two modes mentioned above. Here we can thus compare our observational results directly to theoretical predictions. In addition, we can explore the effect of the RASS flux limit selection on our observational sample.

Fanidakis et al. (2013) present the typical DMH masses for AGNs observed in a redshift range of $z = 0-1.3$. Here we repeat this simulation in a redshift range of $z = 0.16-0.36$, identical to the redshift range used for the observed X-ray and optically selected AGN samples. For each galaxy, the simulation allows one to identify when the AGN is active. An object is included in the AGN sample if its central engine is active in at least one of the five logarithmically spaced snapshots output between $z = 0.16-0.36$. AGN properties such as M_{BH} , L_{bol} , L/L_{EDD} , and redshift are available for each of the different snapshots. The parameter L_{bol} is calculated assuming that the accretion flow forms a geometrically thin disk for relatively high accretion rates (Shakura & Sunyaev 1973). At lower accretion rates, a geometrically thick disk or an advection-dominated accretion flow is modeled (ADAF, Narayan & Yi 1994).

X-ray luminosities are calculated directly from L_{bol} by applying the bolometric correction from Marconi et al. (2004). We consider an object to be an AGN if its intrinsic 2–10 keV rest-frame luminosity is $L_{2-10 \text{ keV}} \geq 10^{41.5} \text{ erg s}^{-1}$. The sample contains X-ray unabsorbed and absorbed AGNs. Based on the luminosity, we use the empirical formula of Hasinger (2008) to determine the probability that the object is absorbed. We then classify statistically if an object is unabsorbed or absorbed. Below, we will refer to this AGN sample as the “all simulated AGN” sample. More recent estimates of the obscured fraction of AGNs as a function of luminosity have been presented by Merloni et al. (2014), who show that the probability that an AGN at high luminosities is absorbed is higher than that suggested by Hasinger (2008). We test the impact of a higher obscured fraction at high luminosities and find insignificant differences as far as clustering measurements are concerned. We therefore retain the empirical obscuration relation of Hasinger (2008) as presented in Fanidakis et al. (2013).

Since RASS is essentially a flux-limited survey (see also Fig. 14, right), only AGNs above a certain X-ray flux are contained in the RASS AGN catalog. However, due to the characteristics of the RASS, different regions of the sky have different exposure times. To mimic the RASS flux selection, we also apply an average flux cut to the simulated AGN sample by using the X-ray luminosities and redshifts of objects in the simulation. We refer to this sample as the “RASS-selected AGN sample.” Its location in the M_{BH} versus L/L_{EDD} plane is shown in Fig. 15 (colored grid points). This sample also includes the effect that RASS is sensitive only to unabsorbed X-

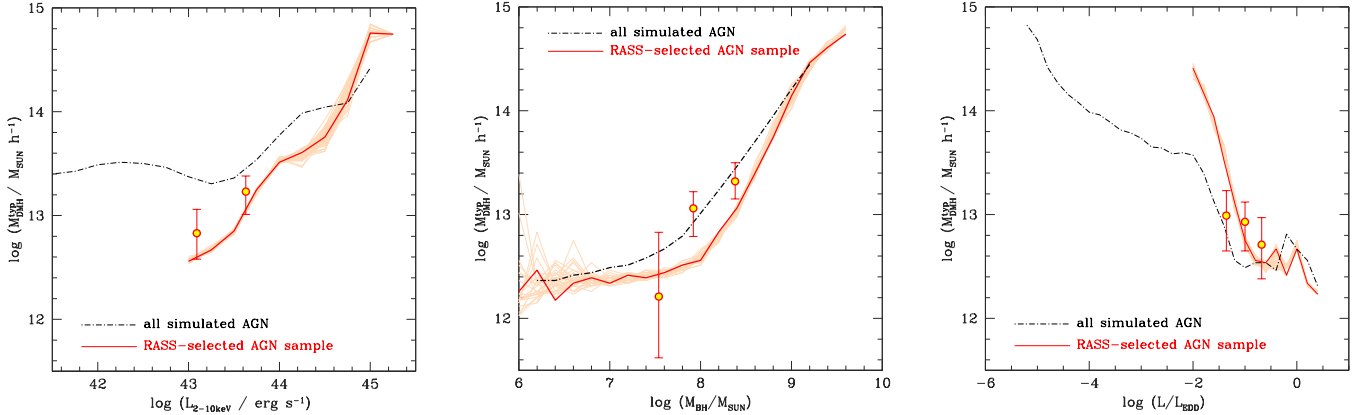


FIG. 16.— *Left*: comparison between the predicted (lines) and observed (data points) RASS AGN typical host dark matter halo mass as a function of hard (2–10 keV) X-ray luminosity. The red line shows the prediction of a simulated RASS flux-limited sample (and $\log(L/L_{\text{EDD}}) > -2$), and the black dash-dotted line shows the expected dark matter halo mass for the total (unbiased) AGN sample with $L_{2-10\text{ keV}} \geq 10^{41.5} \text{ erg s}^{-1}$. We recalculate the relations after adding a random error from a Gaussian distribution with $\sigma = 0.3$ dex to the simulated SMBH masses. We run 50 such realizations; a random subset of these is shown here as orange lines. The data points are plotted at the corresponding median $L_{2-10\text{ keV}}$ values of the observed low and high AGN subsamples (see Table 1, using the conversion presented in Sect. 2.2). *Middle*: similar to the left panel, here showing the predicted and observed halo mass as a function of M_{BH} . *Right*: similar to the left panel, here showing the predicted and observed halo mass as a function of Eddington ratio (L/L_{EDD}).

ray AGNs. However, since the luminosities of the RASS AGNs are high, the simulation classifies the vast majority of the objects as X-ray unabsorbed.

In the same plane, we also show the observed X-ray-selected broad-line RASS/SDSS AGN sample. In general, the simulation agrees well with the observations, in that sources lie in a similar region of this space. However, the simulation slightly overestimates the number of AGNs with $M_{\text{BH}} > 10^{8.5} M_{\odot}$ and $\log(L/L_{\text{EDD}}) < -2$. Such objects should be detectable given the RASS flux limit, but they do not exist in large numbers (at the observed redshift range). However, these are the objects in the simulation for which the accretion flow is modeled with an ADAF. These AGNs are observationally associated with radio-bright, mechanical feedback-dominated SMBHs (e.g., Churazov et al. 2005; Hickox et al. 2009; Smolcic 2009). The optical spectra of these objects do not contain any high excitation lines typical of AGNs (e.g., Best & Heckman 2012). Thus, one might argue that these objects would not be classified as AGNs in an SDSS spectrum. We therefore limit the simulated RASS-selected AGN sample (and the predictions in the following paragraphs) to those sources with $\log(L/L_{\text{EDD}}) > -2$.

Despite these minor differences, we calculate the bias parameter for the simulated AGNs and the observed RASS-selected AGN sample. The bias is calculated in bins of 0.2 in $\log(M_{\text{BH}}/M_{\odot})$ and $\log(L/L_{\text{EDD}})$ using Eq. 4 given in Fanidakis et al. (2013) (see also Eq. 8 in this paper). We follow the same procedure as for the observed AGN samples. Thus, the bias values are converted into typical DMH masses ($\log M_{\text{DMH}}^{\text{typ}}$). Since the simulation uses the conversion given by Sheth et al. (2001) without applying the improved fitting formula by Tinker et al. (2005), we recompute for the observed L_X , M_{BH} , and L/L_{EDD} AGN subsamples in Table 1 $M_{\text{DMH}}^{\text{typ}}$ based only on the ellipsoidal collapse model of Sheth et al. (2001). This allows us to directly com-

pare the predictions with the observations, as shown in Fig. 16.

In the case of the simulated RASS-selected AGN sample, we also assign to every BH mass a random error from a Gaussian distribution with $\sigma = 0.3$ dex. We recalculate all of the relations (red lines) shown in Fig. 16 for 50 realizations and show a subset of these as orange lines. This exercise does not only allows for a more realistic comparison to the data, but also allows us to explore the impact of the intrinsic scatter of approximately 0.3 dex in the M_{BH} estimate of the observed sample. Fig. 16 shows that the 0.3 dex uncertainty in the BH mass estimates has no significant impact on the prediction of the correlations shown. Only at very low M_{BH} and high L/L_{EDD} does the scatter between different realizations increase. However, this is caused by the low number of objects with such properties in the simulations.

For the all-simulated AGN sample (black line), the simulation predicts a positive clustering dependence on X-ray luminosity only above $\log(L_{2-10}/[\text{erg s}^{-1}]) \sim 44$. This might explain why studies of moderate X-ray luminosity do not see a clustering dependence on luminosity and conflicting results are presented in the literature. The RASS selection results in a luminosity dependence that extends down to $\log(L_{2-10}/[\text{erg s}^{-1}]) \sim 43$ (red line). The data and the predictions for the RASS sample agree remarkably well.

For the M_{BH} clustering dependence (Fig. 16, middle), the simulation predicts a strong clustering dependence with M_{BH} for the all simulated AGN sample; a steady increase of typical DMH mass with M_{BH} is found (see also Fig. 7 in Fanidakis et al. 2012). Above $M_{\text{BH}} \sim 10^8 M_{\odot}$ the correlation is even stronger. The RASS flux limit selection of the all-simulated AGN sample has a moderate impact on the M_{BH} clustering dependence. It amplifies the correlation at $M_{\text{BH}} \gtrsim 10^8 M_{\odot}$ and weakens it below $M_{\text{BH}} \sim 10^8 M_{\odot}$ compared to an unbiased AGN sample. The model shows that, in flux-limited samples be-

low $M_{\text{BH}} \sim 10^8 M_{\odot}$, no clustering correlation with M_{BH} should be detectable, although an unbiased AGN sample will still show a very weak M_{BH} clustering dependence in this M_{BH} range. This is consistent with the result found by Komiya et al. (2013).

The observed M_{BH} clustering dependence agrees reasonably well with the model prediction. The data hint that the observed clustering dependence might not be as strong as predicted by the simulated RASS-selected AGN sample.

The predicted L/L_{EDD} clustering dependence also matches the observations well (Fig. 16, right). Below $L/L_{\text{EDD}} \sim 10^{-2}$ the model predicts higher DMH masses than are currently detected for AGNs, but our data do not probe Eddington ratios that low. The model predicts that, at low L/L_{EDD} values, the RASS flux limit selection should cause a very strong negative L/L_{EDD} dependence to the clustering amplitude. The data point with the lowest L/L_{EDD} in the RASS/SDSS AGN sample does not allow us to verify or reject this prediction. Although our samples contain objects down to $L/L_{\text{EDD}} \sim 10^{-2}$ (see Fig. 4), AGN samples with even lower L/L_{EDD} are needed to critically test the prediction of high M_{DMH} at low L/L_{EDD} .

Such tests between observations and state-of-the-art simulations offer a unique opportunity to constrain the physical mechanisms included in galaxy and AGN formation models. For example, a mechanism for the hot-halo mode in which black holes with low L/L_{EDD} and high M_{BH} reproduce the real RASS-selected sample might agree better with the observed AGN clustering dependences. Thus, a channel has to be found to remove the simulated objects with $M_{\text{BH}} \gtrsim 10^{8.5} M_{\odot}$ and $\log(L/L_{\text{EDD}}) \lesssim -2$. In the current model, the hot-halo AGNs arise from the necessity for AGN feedback in massive DMHs. The accretion rate in this mode is calculated indirectly from the cooling properties of the host halo and corresponds to an accretion flow that is able to reproduce powerful AGN outflows that suppress gas cooling and star formation. The tuning of the free parameters in this calculation is done by fitting the model to the observed galaxy luminosity function at $z = 0$. Obviously, more observational data are needed to constrain the model. The comparison between the simulated and real RASS-selected AGN samples in Figs. 15 and 16 could be used as additional constraints for constraining the free parameters in the model.

When cosmological simulations such as the one presented here are adjusted to match the observed AGN clustering properties, to be considered successful they still have to match other observational constraints, such as the luminosity function of galaxies and AGNs at different redshifts. Changes in the physical treatment of AGN accretion might also solve other challenges such as the observed deficiency of low-luminosity AGN at high redshifts when compared to predictions from simulations (e.g., Miyaji et al. 2015). Including various constraints from galaxy and AGN clustering measurements has thus the power not only to improve the simulations but also to enhance our general understanding of AGN physics and AGN and galaxy coevolution.

7. CONCLUSIONS

Motivated by the detection of a weak X-ray luminosity dependence of the clustering strength of AGNs in the first paper of this series, here we explore the physical origin of this dependence. Using the optical spectra of our soft X-ray-selected (RASS/SDSS) luminous, broad-line AGN sample at $0.16 < 0.36$, we estimate black hole masses and Eddington ratios and calculate the clustering dependence on each.

Since M_{BH} and L/L_{EDD} are correlated, we create subsamples in M_{BH} and L/L_{EDD} that have matched distributions in the other parameter of interest. We compute the clustering strength for the subsamples and find a weak clustering dependence with M_{BH} and no significant correlation with L/L_{EDD} . Various adjustments in how the subsamples are created do not change the results. We also study the clustering of the observed parameters (luminosity and FWHM of the broad $\text{H}\alpha$ line) that are used to derive M_{BH} . We find a weak $\text{FWHM}_{\text{H}\alpha}$ clustering correlation in that AGNs with low $\text{FWHM}_{\text{H}\alpha}$ are less clustered than their high $\text{FWHM}_{\text{H}\alpha}$ counterparts.

We also study the clustering properties of an optically selected SDSS AGN sample. This sample has 29% of its objects in common with the X-ray-selected RASS/SDSS AGN sample. We detect the same trends as found for the X-ray AGN sample with respect to M_{BH} , L/L_{EDD} , $L_{\text{H}\alpha}$, and $\text{FWHM}_{\text{H}\alpha}$. The X-ray and optically selected AGN samples show divergent clustering signals for the lowest M_i (absolute i -band magnitude) samples. We argue that this is caused by various complex selection effects in the optical sample and that the X-ray-selected RASS/SDSS AGN sample is more uniformly selected.

From our correlation function measurements, we conclude that M_{BH} is the origin of the observed weak X-ray luminosity clustering dependence. The confidence contours of our AGN HOD modeling parameters further support this finding, as low and high M_{BH} and L_X samples show extremely similar contours, while the low and high L/L_{EDD} sample contours differ significantly from the L_X contours.

The M_{BH} clustering dependence is detected at a significance level of 2.7σ . In both the X-ray and optical AGN samples, the highest clustering strength is found for AGNs with the 30% highest M_{BH} . Thus, at a redshift range of $0.16 < z < 0.36$ luminous broad-line AGNs with more massive M_{BH} reside, on average, in more massive DMHs. In this context, the DMH mass refers to the single largest (parent) halo mass.

Since the observed clustering strength does not depend on L/L_{EDD} in a statistically significant way, AGNs with high accretion rates do not require large-scale dense environments with high galaxy density. This provides evidence that major or minor mergers play only a limited role in the AGN accretion processes in the low-redshift Universe. Internal processes such as disk instabilities could be the dominant AGN triggering mechanism at late cosmic times.

Empirically motivated models that include simple monotonic relationships between M_{DMH} , M_{stellar} , and M_{BH} and without AGN feedback or treatments of AGN triggering do not match well the observed relationships between M_{BH} and M_{DMH} derived from clustering. Thus, we use a semianalytical model to study the predicted clustering dependences as a function of L_X , M_{BH} , and L/L_{EDD} . This model included AGN feedback and two

modes of AGN accretion and fits the observed M_{BH} vs. M_{DMH} relation better than the simple model. Comparing the simulated full AGN sample with a simulated RASS flux-limited AGN sample, we show that observational selection effects moderately change the expected clustering dependences. The simulation predicts that higher M_{BH} are found in more massive halos, and the predicted correlations with L_X , M_{BH} , and L/L_{EDD} agree reasonably well with our observations presented here.

Clustering measurements with small uncertainties offer a unique opportunity, after considering the effects of selection biases, to identify missing physics in our current understanding of the galaxy and AGN evolution by comparing theoretical predictions with observations. Thus, future clustering measurements as a function of various galaxy and AGN parameters will deliver needed additional constraints that will improve upon and distinguish between current theoretical models.

8. ACKNOWLEDGMENTS

We would like to thank Andreas Schulze, Scott Croom, and Antonis Georgakakis for helpful discussions. We also like to thank Peter Behroozi for providing the relation between galaxy stellar mass and dark matter halo mass at $z \sim 0.3$.

This work has been supported by DFG grant KR 3338/3-1, NASA grant NNX07AT02G, CONA-CyT Grant Científica Básica #179662, UNAM-DGAPA Grants PAPIIT IN104113 and IN109710. The research leading to these results has received funding from the

European Community's Seventh Framework Programme (/FP7/2007-2013/) under grant agreement No 229517. ALC acknowledges support from NSF CAREER award AST-1055081.

The *ROSAT* Project was supported by the Bundesministerium für Bildung und Forschung (BMBF/DLR) and the Max-Planck-Gesellschaft (MPG). Funding for the Sloan Digital Sky Survey (SDSS) has been provided by the Alfred P. Sloan Foundation, the participating institutions, the National Aeronautics and Space Administration, the National Science Foundation, the U.S. Department of Energy, the Japanese Monbukagakusho, and the Max Planck Society. The SDSS Web site is <http://www.sdss.org/>.

The SDSS is managed by the Astrophysical Research Consortium (ARC) for the Participating Institutions. The participating institutions are The University of Chicago, Fermilab, the Institute for Advanced Study, the Japan Participation Group, The Johns Hopkins University, Los Alamos National Laboratory, the Max-Planck-Institute for Astronomy (MPIA), the Max-Planck-Institute for Astrophysics (MPA), New Mexico State University, University of Pittsburgh, Princeton University, the United States Naval Observatory, and the University of Washington.

This research also made use of a computing facility available from Departamento de Supercómputo, DGSCA, UNAM.

REFERENCES

- Allevato, V., Finoguenov, A., Cappelluti, N., et al. 2011, *ApJ*, 736, 99
- Anderson, S.F., Margon, B., Voges, W., et al. 2007, *AJ*, 133, 313
- Anderson, S.F., Voges, W., Margon, B., et al. 2003, *AJ*, 126, 2209
- Arnaud, K.A. 1996, *ASPC*, 101, 17
- Avni, Y. & Bahcall, J.N. 1980, *ApJ*, 235, 694
- Behroozi, P.S., Wechsler, R.H., and Conroy, C. 2013, *ApJ*, 770, 57
- Benson, A. 2012, *NewA*, 17, 175
- Bentz, M.C., Peterson, B. M., Netzer, H., et al. 2009, *ApJ*, 697, 160
- Best, P.N. & Heckman, T.M. 2012, *MNRAS*, 421, 1569
- Blanton, M.R., Schlegel, D.J., Strauss, M.A., et al. 2005, *AJ*, 129, 2562
- Bonoli, S., Marulli, F., Springel, V., et al. 2009, *MNRAS*, 396, 423
- Bonoli, S., Shankar, F., White, S.D.M., Springel, V., Wyithe, J.S.B., 2010, *MNRAS*, 404, 399
- Booth, C.M. & Schaye, J. 2010, *MNRAS*, 405, L1
- Brotherthon, M.S., Wills, B.J., Francis, P.J., et al. 1994, *ApJ*, 430, 495
- Bryan, G.L., Norman, M.L., O'Shea, B.W., et al. 2014, *ApJS*, 211, 19
- Cappelluti, N., Ajello, M., Burlon, D., et al. 2010, *ApJL*, 716, L209
- Churazov, E., Sazonov, S., Sunyaev, R., et al. 2005, *MNRAS*, 363, L91
- Coil, A. L., Georgakakis, A., Newman, J. A., et al. 2009, *ApJ*, 701, 1484
- Coil, A. L., Hannawi, J.F., Newman, J.A., Cooper, M.C., Davis, M. 2007, *ApJ*, 654, 115
- Coil, A. L., Newman, J. A., Cooper, M. C., et al. 2006, *ApJ*, 644, 671
- Coil, A. L., Newman, J. A., Croton, D., et al. 2008, *ApJ*, 672, 153
- Cole, S., Lacey, C.G., Baugh, C.M., Frenk, C.S. 2000, *MNRAS*, 319, 168
- Colless, M., Dalton, G., Maddox, S., et al. 2001, *MNRAS*, 328, 1039
- Conroy, C. & White, M. 2013, *ApJ*, 762, 70
- Davis, M. & Peebles, P.J.E. 1983, *ApJ*, 267, 465
- Degraff, C., Di Matteo, T., Springel V. 2010, *MNRAS*, 402, 1927
- Denney, K. D., Peterson, B. M., Dietrich, M., Vestergaard, M., & Bentz, M. C. 2009, *ApJ*, 692, 246
- Eisenstein, D. J., Annis, J., Gunn, J. E., et al. 2001, *AJ*, 122, 2267
- Fanidakis, N., Baugh, C.M., Benson, A.J., et al. 2011, *MNRAS*, 410, 53
- Fanidakis, N., Baugh, C.M., Benson, A.J., et al. 2012, *MNRAS*, 419, 2797
- Fanidakis, N., Georgakakis, A., Mountrichas, G., et al. 2013, *MNRAS*, 435, 679
- Fanidakis, N., Macciò, A.V., Baugh, C.M., Lacey, C.G., Frenk, C.S., 2013, *MNRAS*, 436, 315
- Ferrarese, L. & Merritt, D. 2000, *ApJL*, 539, L9
- Gebhardt, K., Bender, R., Bower, G., et al. 2000, *ApJL*, 539, L13
- Gilli, R., Daddi, E., Zamorani, G., et al. 2005, *A&A*, 430, 811
- Gilli, R., Zamorani, G., Miyaji, T., et al. 2009, *A&A*, 494, 33
- Greene, J. E. & Ho 2005, *ApJ*, 630, 122
- Georgakakis, A., Mountrichas, G., Salvato, M., et al. 2014, *MNRAS*, 443, 3327
- Grupe, D., Komossa, S., Leighly, K.M., Page, K.L. 2010, *ApJS*, 187, 64
- Hamilton, A. J. S. & Tegmark, M. 2004, *MNRAS*, 349, 115
- Hasinger, G. 2008, *A&A*, 490, 905
- Hickox, R.C., Jones, C., Forman, W.R., et al. 2009, *ApJ*, 696, 891
- Hickox, R.C., Mullaney, J.R., Alexander, D.M., et al. 2014, *ApJ*, 782, 9
- Hirschmann, M., Dolag, K., Saro, A., et al. 2014, *MNRAS*, 442, 2304
- Hopkins, P.F., Hernquist, L., Cox, T.J., et al. 2006, *ApJS*, 163, 50
- Hopkins, P.F., Hickox, R., Quataert, E., Hernquist, L. 2009, *MNRAS*, 398, 333
- Kaspi, S., Smith, P. S., Netzer, H., et al. 2000, *ApJ*, 533, 631
- Komiya, Y., Shirasaki, Y., Ohishi, M., Mizumoto, Y. 2013, *ApJ*, 775, 43
- Kormendy, J., Bender, R., & Cornell, M.E. 2011, *Nature*, 469, 374
- Kormendy, J. & Ho, L.C. 2013, *ARA&A*, 51, 511

- Koutoulidis, L., Plionis, M., Georgantopoulos, I., Fanidakis, N. 2013, *MNRAS*, 428, 1382
- Krumpe, M., Lamer, G., Markowitz, A., & Corral, A. 2010b, *ApJ*, 725, 2444
- Krumpe, M., Miyaji, T., & Coil, A. L. 2010a, *ApJ*, 713, 558 (Paper I)
- Krumpe, M., Miyaji, T., Coil, A. L., & Aceves, H. 2012, *ApJ*, 746, 1 (Paper III)
- Krumpe, M., Miyaji, T., & Coil, A. L., 2014, in the Tenth International Workshop on Multifrequency Behaviour of High Energy Cosmic Sources, Clustering Measurements of Broad-*AGNs*: Review and Future, *Acta Polytechnica CTU*, 1, 71
- Landy, S.D. & Szalay, A.S. 1993, *ApJ*, 412, 64
- Larson, D., Dunkley, J., Hinshaw, G., et al. 2011, *ApJS*, 192, 16
- Li, C., Kauffmann, G., Wang, L., et al. 2006, *MNRAS*, 373, 457
- Lusso, E., Comastri, A., Vignali, C., et al., 2010, *A&A*, 512, 34
- Madgwick, D.S., Hawkins, E., Lahav, O., et al. 2003, *MNRAS*, 344, 847
- Malbon, R.K., Baugh, C.M., Frenk, C.S., Lacey, C.G. 2007, *MNRAS*, 382, 1394
- Marconi, A., Risaliti, G., Gilli, R., et al. 2004 *MNRAS*, 351, 169
- Marulli, F., Bonoli, S., Branchini, E., Moscardini, L., Springel, V. 2008, *MNRAS*, 385, 1846
- McGaugh, S.S., Schombert, J.M., Bothun, G.D., de Blok, W.J.G., 2000, *ApJ*, 533L, 99
- McGill, K.L., Woo, J.-H., Treu, T., et al. 2008, *ApJ*, 673, 703
- McLure, R.J., Dunlop, J.S. 2004, *MNRAS*, 352, 1390
- Meneux, B., Guzzo, L., de la Torre, S., et al. 2009, *A&A*, 505, 463
- Meneux, B., Le Fèvre, O., Guzzo, L., et al. 2006, *A&A*, 452, 387
- Merloni, A., Bongiorno, A., Brusa, M., et al. 2014, *MNRAS*, 437, 3550
- Miyaji, T., Hasinger, G., Salvato, M., et al. 2015, *ApJ*, 804, 104
- Miyaji, T., Krumpe, M., Coil, A. L., & Aceves, H. 2011, *ApJ*, 726, 83 (Paper II)
- Mostek, N., Coil, A.L., Cooper, M., et al. 2013, *ApJ*, 767, 89
- Mountrichas, G., Georgakakis, A. 2012, *MNRAS*, 420, 514
- Mountrichas, G., Georgakakis, A., Finoguenov, A., et al. 2013, *MNRAS*, 430, 661
- Mullaney, J.R., Alexander, D.M., Fine, S. et al. 2013, *MNRAS*, 433, 622
- Narayan, R. & Yi, I. 1994, *ApJ*, 428, 13
- Norberg, P., Baugh, C. M., Hawkins, E., et al. 2002, *MNRAS*, 332, 827
- Onken, C. A., Ferrarese, L., Merritt, D., et al. 2004, *ApJ*, 615, 645
- Peebles, P. J. E. 1980, *The Large-Scale Structure of the Universe*, (Princeton, NJ: Princeton Univ. Press)
- Peterson, B.M., & Wandel, A. 2000, *ApJL*, 540, L13
- Porciani, C., Magliocchetti, M., & Norberg, P. 2004, *MNRAS*, 355, 1010
- Richards, G. T., Fan, X., Newberg, H. J., et al. 2002, *AJ*, 123, 2945
- Richards, G. T., Lacy, M., Storrie-Lombardi, L. J., et al. 2006a, *ApJS*, 166, 470
- Richards, G. T., Strauss, M.A., Fan, X., et al. 2006b, *AJ*, 131, 2766
- Rosen, S.R., Webb, N.A., Watson, M.G., et al. 2015, *subm. A&A*, arXiv:1504.07051
- Ross, N. P., Shen, Y., Strauss, M. A., et al. 2009, *ApJ*, 697, 1634
- Salviander, S., Shields, G.A., Gebhardt, K. et al. 2007, *AJ*, 662, 131
- Schneider, D.P., Richards, G.T., Hall, P.B., et al. 2010, *AJ*, 139, 2360
- Schulze, A., Wisotzki, L., & Husemann, B. 2009, *A&A*, 507, 781
- Schulze, A., & Wisotzki, L. 2010, *A&A*, 516, A87
- Shakura, N.I. & Sunyaev, R.A. 1973, *A&A*, 24, 337
- Shen, Y., Greene, J.E., Strauus, M.A. et al. 2008, *ApJ*, 680, 169
- Shen, Y., Strauss, M. A., Ross, N. P., et al. 2009, *ApJ*, 697, 1656
- Sheth, R.K., Mo, H.J., & Tormen, G. 2001, *MNRAS*, 323, 1
- Skibba, R.A., Coil, A.L., Mendez, A.J., et al. 2015, *ApJ*, 807, 152
- Skibba, R.A., Smith, S.M., Coil, A.L., et al. 2014, *ApJ*, 784, 128
- Smolcic, V. 2009, *ApJL*, 699, L43
- Springel V. 2005, *MNRAS*, 364, 1105
- Steinborn, L.K., Dolag, K., Hirschmann, M., Alमुdena Prieto, M., Remus, R.-S. 2015, *MNRAS*, 448, 1504
- Stern, J., & Laor, A., 2012, *MNRAS*, 423, 600
- Sulentic, J.W., Marziani, P., Zamanov, R. et al. 2002, *ApJ*, 556, L71
- Tananbaum, H., Avni, Y., Branduardi, G., et al. 1979, *ApJ*, 234, L9
- Tinker, J.L., Weinberg, D.H., Zheng, Z., & Zehavi, I. 2005, *ApJ*, 631, 41
- Tully, R. B. & Fisher, J. R. 1977, *A&A*, 54, 661
- Ueda Y., Akiyama, M., Ohta, K., Miyaji, T., 2003, *ApJ*, 598, 886
- Vestergaard, M. 2002, *ApJ*, 571, 733
- Voges, W., Aschenbach, B., Boller, T., et al. 1999, *A&A*, 349, 389
- Volonteri, M., Natarajan, P., Gültekin, K. 2011, *ApJ*, 737, 50
- Wake, D.A., Croom, S.M., Sadler, E.M., Johnston, H.M., 2008, *MNRAS*, 391, 1674
- Yang, Y., Mushotzky, R. F., Barger, A. J., & Cowie, L. L. 2006, *ApJ*, 645, 68
- Zehavi, I., Zheng, Z., Weinberg, D. H., et al. 2005b, *ApJ*, 630, 1
- Zehavi, I., Zheng, Z., Weinberg, D. H., et al. 2010, *ApJ*, 736, 59
- Zhang, S., Wang, T., Wang, H., Zhou, H. 2013, *ApJ*, 773, 175
- Zheng, Z., Zehavi, I., Eisenstein, D. J., Weinberg, D. H., & Jing, Y. P. 2009, *ApJ*, 707, 554